THESIS FOR THE DEGREE OF DOCTOR OF PHILOSOPHY

Nanopowder as sintering aid for water-atomized ferrous powder

SWATHI KIRANMAYEE MANCHILI

Department of Industrial and Materials Science
CHALMERS UNIVERSITY OF TECHNOLOGY
Gothenburg, Sweden, 2021

Nanopowder as sintering aid for water-atomized ferrous powder

Swathi Kiranmayee Manchili

ISBN 978-7905-539-4

Doctoral Thesis at Chalmers University of Technology
New serial no: 5006
ISSN 0365-718X

Department of Industrial and Materials Science
Chalmers University of Technology
SE-412 96 Gothenburg
Sweden
Tel: +46 (0)31 772 1000

Printed by Chalmers Reproservice
Gothenburg, Sweden 2021

To my parents!

Nanopowder as sintering aid for water-atomized ferrous powder

Swathi Kiranmayee Manchili
Department of Industrial and Materials Science
Chalmers University of Technology

Abstract

Press and sinter powder metallurgy steels are cost-effective solutions for structural applications. There is a constant drive for improvement in the density of these powder metallurgy steels to expand their usage in high-performance applications. In press and sinter powder metallurgy, consolidation is achieved by compaction, while sintering metallurgically bonds the metal particles. One of the promising ways to achieve improved densification during sintering is the addition of sintering activators to the conventional micrometre-sized metal powder. Nanopowder is associated with excess surface energy due to their very high surface-to-volume ratio, thus, this category of materials has enhanced reactivity. Accordingly, micro/nano bimodal powder are known to yield high densities when processed through other manufacturing routes such as metal injection moulding. This thesis explores the possibility of achieving improved densification by means of nanopowder addition as a sintering aid in water-atomized iron powder processed through the press and sinter route.

Before addressing the sintering aspects of micro/nano bimodal powder, surface, and thermal characteristics of nanopowder were investigated. Iron nanopowder was shown to be covered with an iron oxide layer of 3-4 nm. Different models were used for the estimation and the results from X-ray photoelectron spectroscopy and electron microscopy were complemented by those obtained from thermogravimetric analysis. A methodology to measure the thickness of surface oxide on the nanopowder was proposed and applied to other types of nanopowder The oxide layer underwent a single-step reduction process, and complete reduction was achieved below 600 °C when using hydrogen as a reducing agent. The progress of oxide reduction was studied using thermogravimetric and kinetic analysis, and an oxide reduction mechanism was proposed. While the surface oxide of iron nanopowder follows a single step reduction process, the actual reduction process of Fe_2O_3 undergoes a two-step process to form metallic iron. To study sintering, compacts from micro/nano bimodal powder mixtures were prepared to understand the influence of nanopowder addition on densification behaviour. The presence and increase in the amount of nanopowder decreased the compressibility of the blends. Still, the addition of the nanopowder produced a clear influence on sintering behaviour at temperatures as low as 600 °C compared to compacts containing only micrometre-sized powder. It was found that the sintering is activated at temperatures below 700 °C in nanopowder. Sinter response depended on the type of nanopowder used. Finally, nanopowder was added to pre-alloyed steel powder and evaluated for different characteristics, including flowability, mass loss, density, and impact strength. A detailed microstructural study of steel powder fortified with nanopowder indicated the presence of a chemically heterogenous microstructure after sintering, where presence of nanopowder is proposed to play a significant role in the microstructure development.

Keywords: nanopowder, surface oxide, thermal analysis, sintering, hydrogen, dilatometry, water-atomized iron powder, reduction kinetics, master sintering curve, water-atomized steel powder, compaction

PREFACE

This thesis is based on research performed in the Department of Industrial and Materials Science at Chalmers University of Technology under the supervision of Professor Lars Nyborg and Professor Eduard Hryha. This research was performed within the framework of project funding from the Swedish Foundation for Strategic Research. This thesis consists of an introduction, with an emphasis on aspects related to the sintering of powder metallurgy steels and a summary of the research performed, which is detailed in the following appended papers.

List of appended papers

I. Surface analysis of iron and steel nanopowder
Swathi K. Manchili, R. Shvab, A. Zehri, L. Ye, E. Hryha, J. Liu, L. Nyborg
Surface and Interface Analysis, 2018, Vol. 50, pp. 1083-1088
DOI: 10.1002/sia.6465

II. Investigation of surface and thermogravimetric characteristics of carbon coated iron nanopowder
Swathi K. Manchili, J. Wendel, Y. Cao, E. Hryha, L. Nyborg
Surface and Interface Analysis, 2020, Vol. 52, 1045-1049
DOI: 10.1002/sia.6878

III. Analysis of Iron Oxide Reduction Kinetics in the Nanometric Scale Using Hydrogen
Swathi K. Manchili, J. Wendel, E. Hryha, L. Nyborg
Nanomaterials, 2020, Vol. 10, 1276-1293
DOI: 10.3390/nano10071276

IV. Effect of Nanopowder Addition on the Sintering of Water-Atomized Iron Powder
Swathi K. Manchili, J. Wendel, A. Zehri, J. Liu, E. Hryha, L. Nyborg
Metallurgical and Materials Transaction A, 2020, Vol. 51, 4890-4901
DOI: 10.1007/s11661-020-05891-1

V. Sintering of bimodal micrometre/nanometre iron powder compacts - A Master Sintering Curve Approach
Swathi K. Manchili, J. Wendel, E. Hryha, L. Nyborg
Powder Technology, 2021, Vol. 381, 557-568
DOI: 10.1016/j.powtec.2021.06.052

VI. Carbon-coated nanopowder as sintering aid for water-atomized iron powder
Swathi K. Manchili, F. Liu, J. Wendel, E. Hryha, L. Nyborg
Manuscript

VII. Comparative study on the densification of chromium pre-alloyed powder metallurgy steel through nanopowder addition using design of experiments
Swathi K. Manchili, J. Wendel, M. Vattur Sundaram, E. Hryha, L. Nyborg
Results in Materials, 2021, Vol. 10, 100173
DOI: 10.1016/j.rinma.2021.100173

VIII. Evolution of microstructure during sintering in nanopowder added powder metallurgy steel
Swathi K. Manchili, B. Malladi, J. Wendel, M. Vattur Sundaram,
E. Hryha, L. Nyborg
Manuscript

IX. Impact of nanopowder addition on the densification of Cr-Ni-alloyed powder metallurgy steel
Swathi K. Manchili, M. Vattur Sundaram, J. Wendel, E. Hryha, L. Nyborg
Manuscript

Contribution to the appended papers

I: The author planned and performed the experimental work. X-ray photoelectron spectroscopy was performed by Dr Ruslan Shvab. Analysis of results was performed in collaboration with the co-authors. The author wrote the paper in cooperation with the co-authors.

II, III, IV, V, VII: The author planned and performed the experimental work. Analysis of results was performed in collaboration with the co-authors. The author wrote the paper in cooperation with the co-authors.

VI: The author planned and performed the experimental work. Transmission electron microscopy was performed by Professor Fang Liu. Analysis of results was performed in collaboration with the co-authors. The author wrote the paper in cooperation with the co-authors.

VIII: The author planned and performed the experimental work. EBSD was performed by Mr Bala Malladi. Analysis of results was performed in collaboration with the co-authors. The author wrote the paper in cooperation with the co-authors.

IX: The author planned and performed the experimental work. Compaction and chemical analysis were carried out at Höganäs AB by Dr Maheswaran Vattur Sundaram. Analysis of results was performed in collaboration with the co-authors. The author wrote the paper in cooperation with the co-authors.

Publications that are not included in this thesis

I. **Influence of iron nanopowder addition on sintering of water-atomized iron powder**
Swathi K. Manchili, J. Wendel, E. Hryha, L. Nyborg
Proceedings of World Congress on Powder Metallurgy 2018, Beijing, China

II. **Oxide reduction and oxygen removal in water atomized iron powder: a kinetic study**
J. Wendel, S. K. Manchili, E. Hryha, L. Nyborg
Journal of Thermal Analysis and Calorimetry, 2020, Vol 142, 309-320
DOI: 10.1007/s10973-020-09724-6

III. **Evolution of surface chemistry during sintering of water atomized iron and low-alloyed steel powder**
J. Wendel, Swathi K. Manchili, Y. Cao, E. Hryha, L. Nyborg
Surface and Interface Analysis, 2020, Vol. 52, 1061-1065
DOI: 10.1002/sia.6852

IV. **Reduction of surface oxide layers on water atomized iron and steel powder in hydrogen: Effect of alloying elements and initial powder state**
J. Wendel, Swathi K. Manchili, E. Hryha, L. Nyborg
Thermochimica Acta, 2020, 692, 178731
DOI: 10.1016/j.tca.2020.178731

V. **Sintering behaviour of compacted water-atomised iron powder: effect of initial state and processing conditions**
J. Wendel, Swathi K. Manchili, E. Hryha, L. Nyborg
Powder Metallurgy, 2020, Vol. 63, 338-348
DOI: 10.1080/00325899.2020.1833138

Abbreviations

AES	Auger electron spectroscopy
BCC	Body centered cubic
CIP	Cold isostatic pressing
DIL	Dilatometry
DOE	Design of experiments
DSC	Differential scanning calorimetry
DTG	Differential thermogravimetry
EBSD	Electron back-scattered diffraction
EDS	Energy dispersive X-ray spectroscopy
FCC	Face centered cubic
FEG	Field emission gun
HIP	Hot isostatic pressing
IE	Impact energy
IR	Infrared
KAM	Kernel average misorientation
KAS	Kissinger Akahira Sunose
LAGB	Low-angle grain boundaries
LOM	Light optical microscopy
MIM	Metal injection moulding
PIM	Powder injection moulding
PM	Powder metallurgy
HRSEM	High resolution scanning electron microscopy
HRTEM	High resolution transmission electron microscopy
TGA	Thermogravimetric analysis
XPS	X-ray photoelectron spectroscopy
XRD	X-ray diffraction

CONTENTS

CHAPTER 1

INTRODUCTION

1.1 Background and motivation

Powder metallurgy (PM) defined is a manufacturing technology that involves converting starting material to powder, processing the powder to achieve the required shape, and making it useful a given application. The fluid like behaviour of powder helps in a variety of shaping processes and is beneficial for forming numerous objects, ranging from rocket parts to automotive parts. After the shaping operation of transforming powder into a compact, the compact is heated so that the metal particles bond to one another via a sintering process, which gives the object greater strength. Though the shaping process transforms powder into the required shape, it is the sintering during which the particles bond and impart the desirable properties to the component.

Properties like tensile strength, ductility, impact strength and fatigue strength are directly dependent on the density of the component, see Figure 1.

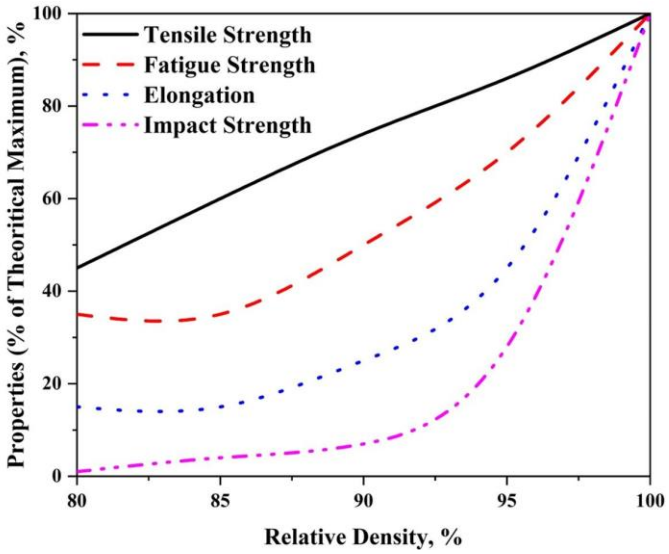

***Figure 1: Representative graph showing the influence of relative density on the mechanical properties of the part** [1].*

For structural applications, improving the mechanical performance of components manufactured through the PM route is of the foremost importance to ensure this method's growth and to enhance its competitiveness with other manufacturing methods. From Figure 1, it is clear that the mechanical properties of a sintered

component are a function of density, and it is therefore essential to improve the density of PM parts. For PM steel components made through the conventional press and sinter route, typical density is in the range of 7.0 to 7.4 g/cm^3, which is less than 95% of the theoretical density. Further improving the density range will allow PM manufacturing to be used for new applications, such as high-performance transmission gears for the automotive industry. Improvement of density either can occur in the core/complete part or can be specific to the surface, depending on the application.

The predominant market for press and sinter structural PM components is in the automotive sector. On average, approximately 80% of all structural PM components for are used for automotive applications, of which the majority are used for transmission purposes [2]. Even if transmissions will change with the development of electrification and hybridization, some reduction from the rotation speed of the electrical engine to the wheels is required, and the loads, torques and requirements on compact design will stoke demand for densification. The most common metal powder grades used are iron, steel, and stainless steel, and iron powder is the mostly produced and consumed substance in the global PM market [3]. Iron powder is produced mainly through the reduction of iron oxide (resulting in so-called 'sponge iron') and water-atomization. Water-atomized and sponge iron powder are therefore the most commonly used powder for structural PM components.

1.2 Research objective

The intention behind improving the density of PM parts is to improve the properties and widen the application of PM to high-performance applications. Densification of PM parts can be either compaction-based, sinter-based or a combination of the two. Sinter-based densification approaches rely on substantial density increases during the sintering phase, which is prominent in the case of metal injection moulding (MIM). There are hybrid approaches like hot isostatic pressing (HIP) in which compaction, creep-assisted and sinter-based densification are realized.

In contrast, press and sinter PM components traditionally rely on what can be referred to as compaction-based densification wherein the components achieve density values close to the final value after compaction and minimal shrinkage occurs during sintering. The density values achievable during compaction depend on the press capacity and powder composition, among other factors, and "maximized" to techno-commercial limits. One approach to achieve further densification would be to exploit the sintering regime. There are different ways in which density can be improved during sintering; namely (a) employing high temperature sintering, (b) maintaining

longer holding time at sintering temperature and (c) using aids to improve densification.

This thesis explores the third approach of using aids to improve densification. Previous studies on sintering-based densification that relies on additives have concentrated on the master alloy approach e.g., [2] [3] [4]. In MIM, research on bimodal powder size distributions has indicated that the addition of nanopowder substantially improves densification during sintering [5]. However, to the best of the author's knowledge, this approach has not been previously studied for the press and sinter steel route.

The objective of this thesis is to clarify the role of nanopowder addition in the sintering of water-atomized ferrous powder for the press and sintering route. Nanopowder is associated with enhanced surface energy which is expected to aid the sintering process. Hence, this thesis aims to study the accelerated sintering process in the presence of nanopowder. In this context, the following research questions are envisaged:

a) *What are the surface characteristics of nanopowder, and how can the surface oxide thickness be determined?*
b) *Which mechanisms are involved in the surface oxide reduction of iron nanopowder, and how can they be evaluated?*
c) *How does the addition of nanopowder influence the compaction and sintering behaviour of water-atomized iron powder?*
d) *How does the addition of nanopowder affect the sintering of steel powder intended for commercial applications?*

1.3 Research strategy

There is substantial effort in the research and development activities in all domains to improve and promote sustainable solutions. In the context of manufacturing, this translates to development leading to increased adaptation of technological solutions that contribute to sustainability. PM is a recognized as a green technology among metal manufacturing processes. To enable rapid adaptation of press and sinter PM parts in areas where these parts are not currently in use, efforts are needed to improve their performance. While full density parts are produced for hot isostatically pressed PM steel, press and sinter PM steel parts typically contain open porosity, which restricts their utilisation because of their lower dynamic properties. HIP requires press and sinter parts to have closed porosity at least on the surfaces. This research thus aims to identify possible alternative routes to achieving closed porosity or near closed porosity to enable capsule-free HIP and to measure these routes' efficacy. With the

same objective, different alternatives are explored for their applicability and efficiency. The present doctoral thesis study constitutes a core part of the efforts of the framework project "Nanotechnology-enhanced sintering steel processing" supported by Swedish Foundation for Strategic Research, involving number of coordinated efforts. One of these is the development and fabrication of steel nanopowder [6]. One completed effort was to identify the densification improvement achievable upon utilization of finer powder for compaction which has been concluded into a previous doctoral thesis study by Wendel with particular reference to the surface oxide reduction mechanisms [7]. The possibility to utilize master alloys and cold isostatic pressing has previously been reported in doctoral thesis by Vattur Sundaram [2]. Also, there are efforts in line to evaluate the performance of gears produced through both conventional route and press and sinter route as part of the framework project, reported recently in a doctoral thesis by Bergstedt [8] along with improved tribo-testing and rolling fatigue tests [9]. Also included in the framework project is cost analysis and sustainability assessment to develop methods and tools for analysing the manufacturing of PM parts in comparison to the conventional production of the same [10].

The present thesis is thus categorized as the main feasibility study to utilize nanopowder as sintering aid. An auxiliary aim is to integrate the parallel development within the framework project to fabricate nanopowder at more rapid production rate compared to normal industrial processes. The final aim of research efforts is to culminate either a synergistic approach or to choose the most efficient among the evaluated process routes to achieve closed porosity and consequently full density after HIP.

CHAPTER 2

POWDER METALLURGY

Powder metallurgy (PM) is a term that covers a wide range of technologies in which metal powder is used for components manufacturing. There are different processes which come under PM including powder forging, hot isostatic pressing (HIP), metal injection moulding (MIM), electric-current-assisted sintering and additive manufacturing, to name a few. The majority of PM products are made through the press and sinter route. In the conventional press and sinter route, powder is converted into the required shape through the application of pressure. This stage is called compaction and the resulting green compact has the correct shape but no strength for the intended application, thus necessitating the high-temperature operation of sintering.

While PM became a mass produced technology in the 20th century, PM is believed to have its beginnings in 3000 B.C, the process of sintering has been known for thousands of years [11]. The carburisation of iron and quenching techniques were used by Ancient Egyptians from 1200 to 700 B.C. Daggers made from gold powder, were used in Egypt in the 14th century B.C. The Delhi iron pillar in India, which weighs 6.5 tonnes, dates to approximately 300 A.D. This pillar was likely processed by hammering or forging reduced iron from iron ore. The PM principles were applied for processing platinum as well due to its high melting point. The modern renaissance of PM can be traced to Coolidge, who used tungsten powder for lamp filaments in the electric lamp by Edison. Considerable development, such as cemented carbides and porous bearings, took place during the late 19th and early 20th centuries. By the 1940s, nuclear fuel elements and many refractories were also manufactured using PM. Today, PM is used in a wide of variety of applications, ranging from dental implants to rocket nozzles and semiconductor substrates. These modern applications depend mostly on manufacturing economy, improved properties, and novel compositions. PM is useful for tailoring the composition to produce a variety of alloy systems that meet specific requirements [12]. Importantly, PM manufacturing is sustainable owing to its high efficiency and the very low material waste it produces (Figure 2).

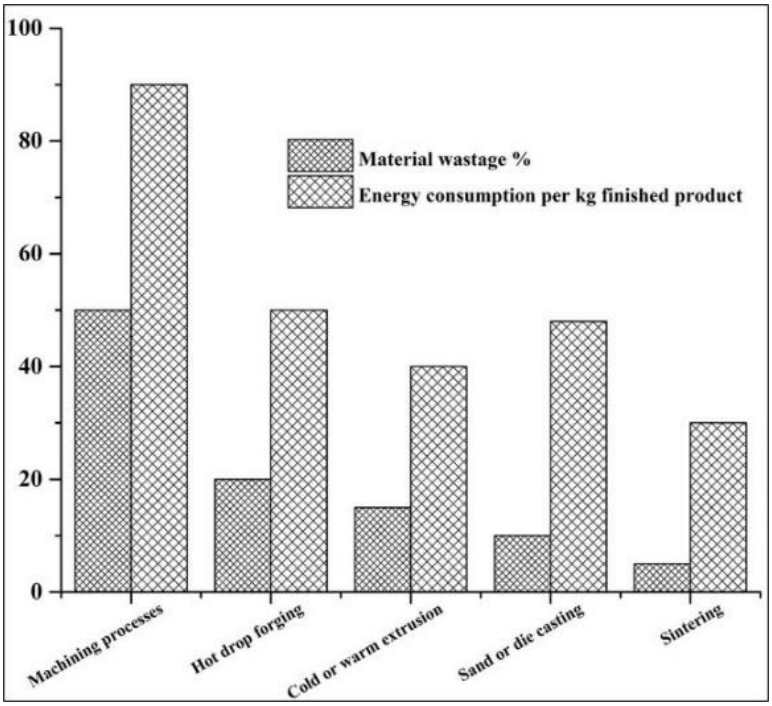

Figure 2: Economic considerations showing how powder metallurgical processing is a sustainable manufacturing technique. Redrawn from [13].

2.1 Different ways to achieve densification

There are multiple ways to achieve densification, but maximum densification is obtained during compaction or sintering. In the conventional press and sinter process, maximum densification is achieved during compaction. Lubricant is necessary for compaction, where typically up to 1 wt.% of lubricant is added; additionally, prior to sintering, delubrication is performed. Sintering builds metallurgical bonds between the metal particles, thereby strengthening the part. In MIM, metal powder is mixed with an organic binder and is injection moulded. The green part is then subjected to binder removal and additional sintering. There is then considerable amount of shrinkage during the sintering stage because a much fine powder is used. Thus, densification results from the sintering stage in MIM. There are also hybrid techniques such as hot isostatic pressing (HIP), where both pressure and temperature act at the same time and contribute to densification. Usually, the powder is filled into a metal container that is evacuated and sealed prior to the HIP process.

Given the above context, this thesis studies the possibility of incorporating a sinter-based densification in an otherwise compaction-based densification press and sinter process through the use of metallic nanopowder as a sintering aid.

2.2 Process chart of powder metallurgy

There are different stages involved in the PM processing route. A typical press and sinter route is presented in the flow chart in Figure 3. The general sequence is as follows: metal powder is blended with lubricant/additives and compacted into the required shape using cold or warm compaction. Warm compaction denotes when the compaction tool and powder are heated to a moderately elevated temperature (maximum 150 °C) [14]. The resultant green compact is then subjected to a high temperature through sintering to impart the necessary strength. After sintering, the component is subjected to secondary or finishing operations depending on its required function. Each of these stages is detailed below.

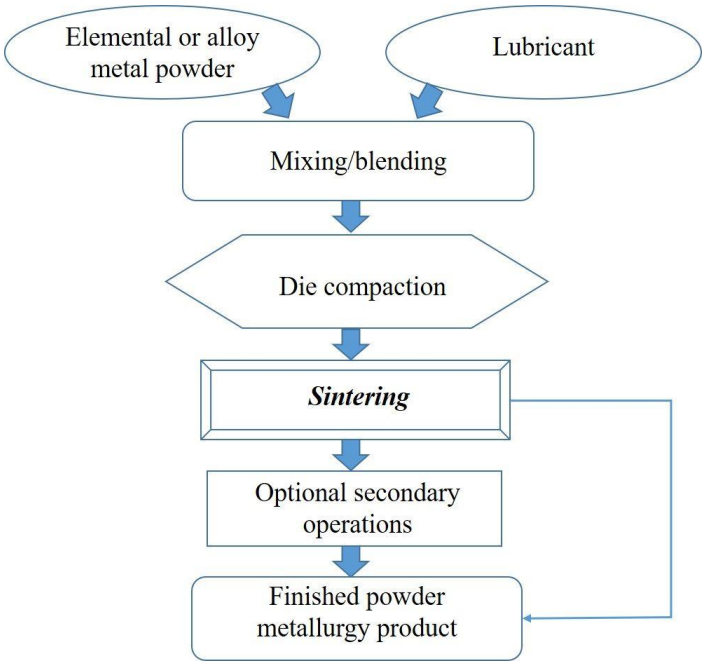

Figure 3: Process chart for powder metallurgy.

2.2.1 Production of metal powder

Metal powder, which is the raw material used in the PM process, can be manufactured in numerous ways. The starting material requires energy to create new surfaces and powder. In the case of metal powder, high energy is needed to create new surfaces, and the process to create these surfaces should be efficient. For structural PM parts, the choice of powder manufacturing technology largely depends on the economic aspects, the required characteristics, and the desired application. Powder production technology can be broadly divided into four types: mechanical, physical-mechanical, chemical and physical-chemical [15] [16].

Grinding, milling and mechanical alloying are considered mechanical processes for powder manufacturing. They are based on the principle of mechanical disintegration, wherein mechanical motion energy is used to create new surfaces. These processes are

solid-state processes where a fracture is initiated and propagated, thus creating new surfaces. Mechanical disintegration can occur through different mechanisms, such as impact, shear, wear, and pressure. In these processes, the smaller the particle, the more difficult it is to apply shear stress for further disintegration, and there is also a probability for re-bonding as the energy associated with small particles is high. Generally, jaw crusher is used for grinding and ball mill is used for milling. One special approach is mechanical alloying. Mechanical alloying is carried out in an attrition mill where a second phase (metal, ceramic, intermetallic, etc.) is uniformly distributed in a metallic matrix; as such, alloying is a result of repeated fracture and cold welding during which the second phase is dispersed.

Physical-mechanical methods include all atomization of melts. The principle behind these methods is the disintegration of the molten melt stream through the application of a gas or fluid jet [17]. Disintegrated molten droplets quickly solidify during the flight due to a rapid cool down. Various shapes of particles are obtained depending on factors like the melt temperature, viscosity, and the cooling conditions. To obtain fine particles, melt viscosity is generally decreased. Alloy powder can also be produced through this process. As rapid cooling is involved, this allows the homogenous distribution of alloy components in the particles. There are different types of atomization processes depending on the type of disintegrating medium used. Water-atomization is when a water jet is used to disrupt the melt stream [18]. Particles obtained through this route are irregular in shape and high in oxygen content. The powder is therefore usually subjected to a reduction annealing step. Water-atomization is economical and has very high productivity and is hence a widely used process for commercial production of metal powder in large tonnages. With high pressure water-atomization, fine particle size distribution can be achieved. In principle, this technology could be used for all metals that can be melted, but it is commercially used primarily for iron, copper, steels, aluminium, tin and lead [19].

Gas-atomization is when the melt stream is disintegrated by air, helium, argon, or nitrogen flowing from the nozzles at a certain pressure. This method is recommended for highly alloyed materials like superalloys and stainless steels. Gas-atomized powder is characterised by its spherical shape and the homogeneity of its chemical composition. Another form of atomization is centrifugal atomization such as the rotating electrode method, in which an arc is located between the alloy electrode, acting as an anode, and a water-cooled tungsten electrode, acting as the cathode. Hence, this is a two-step process involving the melting of the alloy or metal and the centrifugal forces that disintegrate the molten metal or alloy [12]. Melting can occur either through an arc or plasma.

Chemical production methods involve reduction of metal compounds like iron oxides to produce sponge iron powder, WO_3 to form tungsten powder and so forth. The reduction process has significant importance as more than half of iron powder production for PM applications occurs through the reduction of iron oxide. Solid or gaseous reducing agents are used for the reduction process and high temperature is employed. Depending on the reducing agent, there can be either a direct or indirect reduction reaction. One example is the Höganäs process in which iron ore is reduced to so-called sponge iron. The Höganäs sponge iron process is a chemical process in which the finely divided iron ore, magnetite is reduced with coke breeze resulting in a spongy mass of solid metallic ore [20].

Electrochemical production methods can be used for a large number metals, with electrolysis carried out to obtain metal powder from metals such as nickel and copper. Fine spherical powder is dominantly produced through a carbonyl process to produce fine iron and nickel powders.

2.2.2 Powder shaping and compaction

Powder can be moulded into the required shape through a pressure-assisted compaction process. Powder mixed with additives is poured into the die cavity, and the mix is subjected to mechanical loading. The applied pressure leads to the compaction of the powder. There is friction between the metal particles as well as between the metal particles and die walls. Additives in the form of lubricant are added to reduce friction and improve die life. When compacting pressure is applied to the powder, first there is rearrangement which takes places by filling the cavities in between the particles. As pressure increases, the contact area between the particles also increases and the particles are plastically deformed [21]. Depending on the shape of the particles, mechanical interlocking takes place and is normally a necessary part for the green strength of the compacted part. Upon further increase in pressure, there is further increase in the contact area. The metal particles are deformed which makes it difficult to further increase the contact area as they harden.

Apart from die pressing, shaping of powder into a compact can be done by extrusion, forging, rolling or hot/cold isostatic pressing. There are also methods like explosive compaction where powder is compacted via explosive detonation. This is a dynamic and high-energy process that enhances the mechanical properties of the components. Isostatic pressing of the metal powder through the supply of pressurised fluid to create a green body is referred to as cold isostatic pressing (CIP). Metal powder is filled in an elastic container and placed in a pressure chamber. A pressuring fluid creates pressure evenly along the container surface; this helps to press metal powder

together and to create a green body. The benefits of CIP are isotropic compaction, where there is no need for lubricant, and suitability for compacting larger parts more easily.

Another important shaping technique is powder injection moulding (PIM), often referred to as MIM when metal powder is used. The MIM process offers a unique advantage over the conventional press and sinter approach by producing objects with precise dimensional tolerances of shapes that cannot be obtained by press and sinter. MIM is also considered a high-volume manufacturing technology. Apart from pressure-assisted methods, there are also a few pressure-less shaping methods, which are generally used for ceramics but are applicable to metal powder as well. Slurry is then first prepared and methods like slip casting, freeze casting and starch forming are also used [17].

In this thesis study, the conventional press and sinter route was used, and powder was therefore subjected to uniaxial compaction before sintering.

2.2.3 Sintering

Sintering is the next step after powder shaping. It is a process during which strength is imparted to the part through heating to approximately 60% to 90% of the melting temperature. Sintering can be executed in a single step or as a multi-step process, depending on the required function of the part. Before sintering, added lubricant should be removed through a delubrication operation [22].

Sintering is discussed in Chapter 4 in detail.

2.3 Advantages associated with press and sinter powder metallurgy

The PM route can be used to process numerous components, but a few design considerations should be kept in mind when considering PM components [23]. First and foremost, the ejection of the part from the die must be considered. The design should allow the part to be easily ejected from the die. Thin walls, sharp corners or narrow edges must be eliminated because powder flow into such spaces is difficult. Varying wall thickness can be advantageous. Holes at right angles to the pressing direction are not advisable, whereas holes in the direction of pressing are recommended. Undercuts are not advisable as ejection of the part can be difficult.

There must be a good reason for choosing PM over conventional wrought manufacturing processes. There are several reasons that PM is chosen over other manufacturing routes, the most important of which are cost effectiveness and uniqueness of the process. Below are a few advantages [24], [25], [26], [27].

- The PM is considered a mass production technology with very high production rates and carries huge potential for cost savings as price per unit produced is low. It is especially efficient for complex parts produced in large volumes.
- PM is a near-net-shape forming approach, and the processing route involves high material utilization (above 97%) and results in very little scrap.
- The high dimensional accuracy of PM sometimes helps in minimising or avoiding finishing operations as closer dimensional control and with very good surface finish are obtained.
- With PM there is unparalleled flexibility in producing different shapes and compositions which are otherwise not possible with good repeatability.
- A wide variety of metals and non-metals can be processed by means of PM. Hard metals with a high melting point or refractory materials are uniquely obtained by PM with less difficulty and lower costs. Certain products like sintered carbides and porous bearings can be made only through PM processing route.
- Tailored properties can be obtained by means of PM, using a variety of compositions. Desired mechanical and physical properties such as density, hardness, toughness, stiffness, damping, and specific electrical or magnetic properties are tuned to the application versatility. PM results in consistent isotropic properties and dimensions as well as good chemical homogeneity.
- PM is economical as the raw materials are readily available.
- The PM components with controlled inter-connected porosity can be infiltrated with lubricants and used as self-lubricating bearings for special applications. Magnetic components can also be produced by means of PM.

2.3.1 Limitations

Despite of the many advantages of PM, there are also a few limitations ([26], [27], [28], [29])

- The costs of metal powder may outweigh those of the raw materials used for melting.
- Storage of metal powder must be controlled as powder may deteriorate if not handled properly in certain cases.
- The costs of tools and equipment may be high in relation to production volume.

- There are restrictions on part size as large parts are difficult to process through the normal press and sinter route.
- Owing to the inherent porosity of press and sinter parts, there could be lower ductility and fracture toughness in comparison with their wrought counter parts.
- There could be workforce health hazards as the atmosphere can be contaminated with fine metal powder.

CHAPTER 3

FERROUS POWDER METALLURGY

Powder Metallurgy (PM) is an established green technology for mass producing near-net-shape components. Mass production permits lower total costs and minimum material loss, which makes it an attractive manufacturing route. The automotive industry is a major consumer of PM components. Ferrous PM dominates with respect to the total tonnage [30]. About 80% of worldwide production of PM components finds its place in automotive industry. Still, ferrous PM constitutes a small part of the total use of steel in the world. The global consumption of steel is projected to be around 2.8 Gt by 2050 [31], while the consumption of PM by global market stands at 1 Mt per year [32], with the majority of material consumption occurring in the automotive industry. It is important to note that with increasing electrification, conventional press and sinter PM needs to adapt to remain competitive in the industry. In fact, PM is an inherently flexible manufacturing technology with respect to processes, materials, shapes and products [33].

Automobile manufacturers want components to be light-weight and superior in performance and to have enhanced durability and reliability to produce safe vehicles at a low cost. PM offers components with improved performance at a low total cost and greater design flexibility compared to traditional manufacturing routes. Examples of commercial products manufactured from water-atomized powder are complex-shaped conventional press and sinter components, precision parts from fine powder by metal injection moulding (MIM) and bronze bearings from copper-based powder. However, PM faces the challenge of oxidation, especially, for alloys containing elements with high oxygen affinity [34]. Oxidation is also observed on the surface of metal particles in the form of surface oxides. Alloying elements like silicon, manganese and chromium are strong oxide formers and hence prone to form oxides. Researchers analysing stainless steel powder found that its surface oxides were rich in chromium, manganese and silicon compared to bulk alloy content [35]. Generally, annealing is carried out to reduce the oxide content of surfaces of water-atomized iron and steel powder. The shape of the powder through water atomization is generally irregular, unlike the spherically shaped particles that result from gas-atomization (gas is used as a medium to disintegrate the liquid stream). For press and sinter parts, particle shape is important as the green strength of components made of irregularly

shaped particles is higher than that of components with spherical particles due to mechanical interlocking between particles.

Most PM components use powder produced through water or gas-atomization. Water-atomized ferrous powder (iron and low-alloy steel) is used in the manufacturing of most ferrous components due to its relatively low production costs [32] [36]. Most powder production is concentrated in this segment. Carbon, a significant alloying element, is added in the form of graphite to facilitate the required steel composition necessary for the intended strength. Copper is added for both solid solution strengthening and dimensional control purposes. Nickel and molybdenum are added to enhance hardenability and they do not form stable oxides at normal sintering temperatures, whereby their oxides are easy to reduce. Moreover, these alloying elements are discouraged due to price volatility, health concerns regarding the usage of nickel and recyclability issues with copper. Accordingly, there is a push for the use of more sustainable elements.

Alloying elements like chromium and manganese are added, though they form stable oxides at normal sintering temperatures if sintering atmosphere is not properly controlled. This effect can be avoided by increasing sintering temperature or ensuring an appropriate reduction atmosphere during sintering. Chromium has several advantages as an alloying element. Apart from its economic favourability compared to copper and nickel, chromium leads to higher hardenability, which makes it suitable for high-performance applications [22]. However, chromium's high oxygen affinity poses a challenge during processing. To deal with this challenge, pre-alloying is carried out that reduces the activity of chromium without significantly degrading powder compressibility [37]. Two decades ago, Höganäs AB, Sweden, introduced a cost-effective, pre-alloyed, water-atomized steel powder grade called Astaloy CrM containing 3 wt.% Cr and 0.5 wt.% Mo [38]. Chromium pre-alloyed grades like CrM (Fe-3.0Cr-0.5Mo) and CrA (Fe-1.8Cr) introduced by Höganäs AB, Sweden are used for high-performance applications.

There are different ways in which alloying elements are alloyed, including pre-alloying, diffusion alloying, admixing and so on. In pre-alloying, the alloying element is added to the liquid melt before the atomization process. Although this method ensures the homogeneity of the alloying element, it impairs the compressibility of the powder because the alloying element imparts strength to the powder particle. Chromium is commonly pre-alloyed and is thus directly incorporated into the metallic matrix, forming a solid solution [38] [39]. In diffusion alloying, a relatively low temperature treatment is applied to bond the fine particle elemental additions, which are typically up to several dozen micrometres in size, of nickel, molybdenum and

copper bonded to the surface of the iron particles; this ensures that compressibility is retained and also delivers the effects of the additions in a more controlled and predictable manner. Binder-treated mixes are grades where alloying additions adhere to particle surfaces. The addition is carried out using an organic binder that also acts as the pressing lubricant. The alloying additions can be made into an iron base powder in the form of elemental or ferroalloy powders during admixing. As iron powder is unalloyed, it retains compressibility.

For admixing, binder-treated mixing and diffusion alloying, a heterogeneous microstructure is observed after sintering through the diffusion of the alloying elements at given sintering temperatures. Studies conducted on various ferrous PM materials alloyed using different methods indicate that this has a significant influence on the sintering response of a material and on the shape and size of the pores the material has [40].

3.1 Gear manufacturing using PM

Conventional gear manufacturing typically comprises machining and gear cutting from the blank [41]. Gear manufacturing through PM has an inherent advantage in manufacturing complex shapes and profiles in large volumes from a single pressing operation, although final grinding to set the gear profiles may be needed. As noted, PM processing is an economical approach as it generates less raw material wastage and is also energy efficient [42]. However, the presence of pores presents a limitation to using PM products for high-performance applications, especially under dynamic loading conditions [43] [44]. This drawback drives the continuous improvement process to increase the density of PM components. Fatigue properties play a vital role in gears used for heavy-duty and automotive transmissions, and fatigue properties are dependent on porosity features such as pore size, structure and distribution that initiate the surface crack [45] [46].

To improve fatigue properties, post-processing operations like surface rolling are performed to improve surface densification, which in turn increases the load-bearing capacity of PM gears [47]. Another way to increase fatigue properties is by densifying PM components to around 95%, which enables them to reach full density after performing capsule-free hot isostatic pressing (HIP) [48] [2]. In order to carry out capsule-free HIP, it is necessary to close the pores that are open to the surface as any such surface-connected pores that are interconnected will not be densified [49] [50]. Closed pores are efficiently eliminated through HIP to reach full density [51]. For water-atomized steel powder, it has been shown in high temperature sintering studies that the transition from open to closed porosity occurs at around 95% of the theoretical

density [52]. This then sets the pre-conditions to employ container-less HIP, which eliminates the costs related to the HIP capsule. HIP can be also combined with integrated heat treatment and quenching operations [51].

3.2 Surface characteristics of iron and steel powder

The oxygen present in the powder is bound in the form of oxides on the surface as well as internal oxide inclusions in the matrix of the particles, depending on powder composition and manufacturing method. Previous research on the surface characteristics of water-atomized chromium pre-alloyed steel powder have shown that the surface of the powder particle is predominantly covered by 4-6 nm iron-rich oxide layer along with particulate oxides rich in chromium, manganese and silicon that are a few hundred nanometres in size [53] [54] [55] [56]. The iron-rich oxide layer covers more than 90-95% of the particle surfaces [55]. Besides possible internal oxide inclusions, only a very small amount of oxygen may be present in its elemental form in the iron matrix as it is well known that the solubility of oxygen is low in iron matrix.

3.3 Base powder used in this thesis

The base powder used for the experimental work in this thesis are water-atomized iron and steel powder grades produced and supplied by Höganäs AB, Sweden. Pure iron powder (ASC 300) and steel powder (Astaloy CrA) were used as experimental materials. Carbonyl iron powder, which is a fine grade, was used as a base powder in Paper V to benchmark sintering behaviour.

CHAPTER 4

NANOPOWDER

Nanotechnology is a multidisciplinary field in science, which functions at the intersections of physics, chemistry, materials science, and other engineering sciences. This makes it convenient for the application of such technology in almost all branches of science and technology. The term 'nanotechnology' was first used by Professor Norio Taniguchi in 1974, and it became an emerging field in the 1980s. The word 'nano' derives from the Greek word *nanos* and the Latin term *nanus* which means *dwarf*. Nanotechnology can also denote the ability the construction of items from the bottom up using advanced techniques and tools, to create high performance products. In the top-down approach, nano-objects are constructed from larger entities without atomic-level control [57]. The basic elements of nanotechnology are the nanomaterials, which can be defined in different ways. Nanomaterials are popularly defined as materials which are less than 100 nm in one dimension [58]. Applications of nanomaterials include energy storage, energy conversion, solar cells, pharmaceuticals, life science applications, optoelectronics, sensing and actuation nano-systems, catalysis, composite materials, engineering materials, water purification, and so forth.

This chapter classifies the various types of nanomaterials, followed by a brief discussion and synthesis of the different nanomaterials. Novel properties and applications associated with nanomaterials are also addressed.

4.1 Classification

Nanomaterials come in different shapes such as nanorods, nanoparticles and nanosheets, which can be characterised based on their dimensionality [59]. Nanomaterials can be engineered, incidental or from natural sources. Engineered nanomaterials include carbon black, colloidal and synthesised nanoparticles [60] [61]. Nanomaterials that are produced as a by-product of mechanical or industrial processes are incidental nanomaterials, with sources including engine exhausts, welding fumes or combustion processes from domestic solid fuel heating. Incidental atmospheric nanoparticles are referred to as ultrafine particles and contribute to air pollution [62]. Natural nanomaterials are often biological systems like corals, cotton, paper, natural colloids, the bottom of gecko feet, the bone matrix of the human body, clays, and opals.

Nanomaterials can be classified into different categories depending on the number of dimensions they have in nanoscale. These categories include (a) layered or lamellar

structures, (b) filamentary structures and (c) equiaxed nanostructured materials; these categories equate to one-dimensional (1D), two-dimensional (2D) and three-dimensional (3D) nanomaterials, respectively. The thickness of 1D nanomaterials (layered or lamellar structures) is only a few nanometres, whereas the length and width are much greater. For rod-shaped 2D nanomaterials (filamentary structures), length is substantially greater than the width or diameter, which are in nanoscale. Equiaxed structures where all three dimensions are in nanoscale are called 3D nanomaterials. Nanomaterials can be crystalline, quasi-crystalline or amorphous in nature and can be metals, ceramics, polymers or composites [63]. Research concerning synthesis, consolidation and characterisation is focused on 3D nanomaterials and 1D nanomaterials. 3D nanomaterials have numerous applications due to their high strength and formability.

4.2 Synthesis of nanomaterials

Nanomaterials can be synthesised by either consolidating small clusters or breaking down the bulk material into smaller and smaller dimensions [64] [65]. Nanomaterials can be synthesised using various methods, including inert gas condensation, mechanical alloying, spray conversion processing, electrodeposition, physical vapour deposition, chemical vapour deposition, chemical vapour processing and sol-gel processing [63]. Techniques like severe plastic deformation are used to produce very fine-grain-sized materials in bulk form [66]. There are advantages and disadvantages associated with each of these methods, and the appropriate method is selected depending on the requirements of a given part, such as the required microstructural features, chemical composition, surface chemistry or purity. Using ultra-high vacuum conditions to maintain extremely clean surfaces adds to the production costs of nanomaterials. Inexpensive methods for producing nanomaterials include inert gas condensation, mechanical alloying/milling, and electrodeposition.

To use nanomaterials for a wide range of applications, large-scale production of powder is needed. The powder produced is then consolidated into the required shapes. Powder metallurgy (PM) techniques are used for the consolidation of nanopowder, though special precautions are needed to minimise their chemical activity and to deal with high interparticle friction. The aim of consolidation is to achieve fully dense materials that retain the nanostructure without coarsening the material. Using high temperature processes for an extended period of time to achieve full density results in significant coarsening of the nanostructure provided by the nanopowder. Techniques like electro discharge compaction, plasma-activated sintering, explosive consolidation, hot-isostatic pressing, hydrostatic extrusion, powder rolling and sinter forging can be used to consolidate nanopowder [67] [68].

4.3 Characterizing nanomaterials

The characterisation of the physical and chemical properties of nanopowder or nanoparticles is carried out using several techniques; these techniques are sometimes used exclusively for the study of a particular property, while in other cases they are combined [69]. Table 1 summarises parameters determined, and the corresponding characterization techniques employed.

Table 1: Entity assessed along with the corresponding characterisation techniques employed to nanomaterials [70].

Entity characterised	Characterisation technique
Size	Transmission electron microscopy (TEM), dynamic light scattering (DLS), small angle X-ray scattering (SAXS), high resolution transmission electron microscopy (HRTEM), scanning electron microscopy (SEM), atomic force microscopy (AFM)
Shape	TEM, HRTEM, AFM, 3D-tomography
Chemical composition	XRD, X-ray photoelectron spectroscopy (XPS), inductively coupled plasma-mass spectrometer (ICP-MS), inductively coupled plasma-atomic emission spectroscopy (ICP-OES), Energy dispersive spectroscopy (SEM-EDS and TEM-EDS)
Crystal structure	XRD, HRTEM, electron diffraction, scanning transmission electron microscopy (STEM)
Size distribution	DLS, SAXS, SEM
Chemical state	electron energy loss spectroscopy (EELS), XPS
Surface composition	XPS, Fourier transform infrared spectroscopy (FTIR), secondary ion mass spectrometry (SIMS)
3D visualization	3D tomography, AFM

4.4 Properties of nanomaterials

Fully dense parts that retain their nano size using nanomaterials exhibit increased strength/hardness, enhanced diffusivity, reduced density, higher electrical resistivity, increased specific heat, higher coefficient of thermal expansion, lower thermal conductivity and superior soft magnetic properties in comparison to their coarse

counterparts [63], provided that their nano size is preserved when processed into bulk form. Henceforth, the focus in the forthcoming will is on nanopowder, which comes under 3D nanomaterials category.

4.4.1 Diffusion and sinterability

Nanomaterials contain a large fraction of atoms along their boundaries and interfaces, providing a high density of diffusion paths. They are therefore expected to show enhanced diffusibility compared to their coarse counterparts [71], which influences the sintering of nanopowder. Nanopowder with increased diffusibility and surface energy mean that sintering can occur at temperatures that are much lower than those required for coarse powder. For example, titanium aluminide nanopowder can be sintered at temperatures approximately 400 °C lower than the temperature required for coarser powder [68].

The topic of sintering in nanopowder has both scientific and technological importance for the fabrication of bulk materials. As a result of the extremely small size and the high surface to volume ratio, nanoparticles show during sintering a unique behaviour compared to their coarse powder counterparts [72]. However, nanopowder sintering raises fundamental issues that cannot be fully comprehended using conventional theories of sintering. A linear approximation of coarse powder sintering theories cannot be applied to nanopowder sintering when modelling driving force and mass transport equations. Sintering temperatures for nanopowder are also lower than their coarse counterparts, which can be exploited when manufacturing engineering materials from nanopowder. The onset temperature of sintering for most materials can be reduced by more than 200 °C depending on the particle size. For metals that require very high temperatures for sintering, such as tungsten, using nanopowder can reduce sintering temperature drastically.

Grain growth for nanopowder after sintering can be divided into two phases. Initial grain growth consists of dynamic growth resulting from the coarsening of particles via interparticle mass transport; this causes the material to lose its nanocrystalline nature but aids densification. The second part of grain growth consists of normal grain growth reminiscent of that in bulk materials.

4.4.2 Melting of nanopowder

Melting point depression is a property of nanoparticles. Small particles have a lower melting point than their bulk counterparts due to an increased number of surface atoms as particle size decreases [73]. To determine the melting-point depression for nanosized particles, a classical thermodynamics approach was adopted through the use of the Gibbs-Thomson equation as follows [73]:

$$\boldsymbol{T_m(r) = T_m(\infty) - \frac{2T_m(\infty)\sigma_{sl}}{\Delta H_f(\infty)\rho_s r}} \quad \textbf{(1)}$$

where $T_m(\infty)$ is the melting temperature of the bulk material, $\Delta H_f(\infty)$ is the latent heat of fusion of the bulk material, ρ_s is the density of the material in a solid state, r is the radius of the particle, $T_m(r)$ is the melting temperature of a particle with radius r and σ_{sl} is the solid-liquid interfacial energy. The shape of the particle is assumed to be spherical. This equation is a simple way of predicting the relationship between melting temperature and decreasing particle size [73].

4.5 Safety

Nanoparticles should also be characterised using toxicology and exposure assessments to assess their health and safety hazards. The inhalation toxicity of nanoparticles has been researched, see for example [74], and the toxicological profile of nanoparticles has developed further as the usage has increased [75]. Toxicity is important as environmental particulates pollute the air and can have several sources. The finer the particle size, the more severe its adverse effects are; these effects can range from exacerbations of respiratory diseases, pulmonary inflammation or death from respiratory and cardiovascular diseases [76].

4.6 Nanopowder used in the present work

In PM processes, nanopowder has overall advantages over the micrometre range powder. In addition to decreasing sintering temperature, the fine grain structure slightly enhances mechanical properties [77] [78] [79] [80]. Nanopowder is used extensively to produce micro-components through powder injection moulding (PIM) [81] [82] [83]. Un-controlled oxidation caused due to the large surface area and high interparticle friction represent some of the difficulties of processing nanopowder into bulk components [84]. The most critical limitation is the high cost involved as the processing and handling of nanopowder is expensive [77].

In this thesis, nanopowder was used as a sintering aid. However, the size of the nanopowder was too large to observe a significant melting-point depression phenomenon. The Gibbs-Thomson equation was therefore used to calculate the

melting point of the iron nanopowder used in the study (Figure 4). This nanopowder had a size range of 35 to 80 nm. The calculation yielded similar values to the bulk melting point temperature. As such, the size of the nanopowder in this study was too large for melting-point depression to occur. The nanopowder therefore played a role in improving the low temperature sintering of water-atomized ferrous powder instead of being a trigger for melt formation and liquid-phase-assisted sintering. Details of the types of nanopowder used in this thesis are given in the Chapter 6 Materials and Methods.

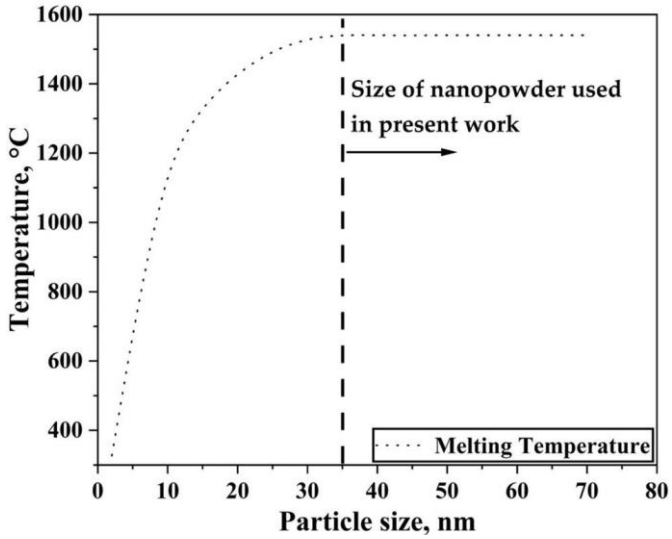

Figure 4: Plot showing Gibbs Thompson calculation for the melting point of iron nanopowder used in this study. The plot predicts that there is no melt point depression.

CHAPTER 5

SINTERING

As mentioned, sintering is a thermal process during which particles bond together and part strength is increased. Better understanding of the sintering process is expected to provide insight into how to improve product quality. Density is used as a measure for degree of sintering and is expressed as g/cm^3 or kg/m^3. The theoretical density of a material is when it is pore-free.

5.1 Definitions of sintering

Sintering has multiple definitions. Sintering can be understood as a thermal treatment for bonding particles into a coherent solid structure via mass transport events that often occur on the atomic scale [85]. In mechanical terms, sintering is a thermally activated transition of a powder or porous system to a more thermodynamically stable state through the decrease of overall surface free energy. Sintering is an operation during which powder in a pre-shaped body obtains the required physical-mechanical properties by changing its structure. Sintering can also be defined as a process by which the powder compact is transformed into a strongly bonded monolithic mass. It can also be understood as a complex process during which particles undergo changes in shape and size when heated to a sufficiently high temperature. As a result, there is a volumetric shrinkage during sintering that leads to densification as pore volume and size are reduced.

5.2 Types of sintering

Approaches to sintering can be broadly divided into solid state and liquid state sintering. Solid-state sintering is when there is direct contact between the particles and overall contact area increases during the process. In liquid phase sintering, the presence of a liquid ensures the adherence of the solid particles. There are a few more types of sintering, such as high-pressure sintering, reactive sintering, microwave sintering and spark plasma sintering, but these relate to different ways of pursuing the sintering process rather than the state of matter being solid or partly liquid.

The key parameters for sintering are temperature, vapour pressure, initial particle size, particle size distribution, heating rate, holding time, presence of agglomerates, green density, uniformity of initial microstructure, atmosphere, and sintering aids. In addition, the material determines the surface energy, activation energy for diffusion and crystal structure. In this thesis, solid state sintering has been studied.

5.3 Theory of sintering

This section presents an overview of the principles and mechanisms associated with powder sintering. This section is summarised based on the work presented in the following studies: [86] [87] [88] [89] [90] [91] [92] [93] [94] [95] [96].

The important question is why do materials sinter or why do the pores reduce in size and amount?

There must be a high temperature or a driving force that triggers metal particles to sinter. This driving force can be seen in two respects; the first is in the macroscopic scale, where the driving force for sintering lowers the excess energy associated with the free surfaces of metal particles. Powder is associated with high specific surface area; that is, the surface area per unit weight is larger in powder than in solid materials. All surfaces are associated with certain amount of surface energy. Thus, metal particles with a very high surface area are associated with excess surface energy. If given an opportunity, the system tries to lower overall surface energy. This reduction in excess surface energy can occur in two ways:

I. Reducing the total surface area by increasing the average size of the particles (coarsening of the particles). Coalescence of fine particles results in reduction of total surface area, but no strong bonds are formed during this process. Generally, this is observed in loose powder sintering. The mechanical strength thus obtained is also very low.
II. Replacing the high-energy solid-vapour interface with a low-energy solid-solid interface (grain boundary formation). Strong bonds are formed between particles, and the solid-vapour interface is replaced by a solid-solid interface through the formation of a grain boundary. There is also an inter-particulate transfer of certain atoms that results in a chemical bond.

Both processes may occur simultaneously, or one can precede the other.

This process can be explained using a simple model, as shown in Figure 5.

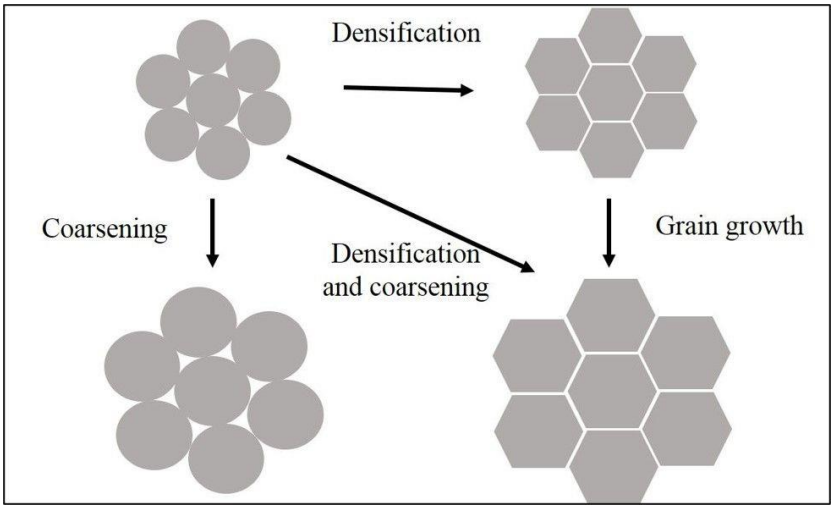

Figure 5: Schematic of particle coarsening and densification.

As shown in Figure 5, when particles are initially loosely bonded, the amount of solid-solid interface is much lower compared to that of the solid-vapour interface. There are three possibilities for what will happen when the system is heated. First, the simple particle coarsening described above may occur. Some particles grow at the expense of others as the mass remains constant, but the contact area does not change significantly as there is no chemical bonding. Thus, there is a change in the surface area term. Overall system energy decreases as the surface energy term reduces, but there is no strength imparted to the material. The second possibility is densification, wherein particle configuration changes to form a strongly bonded structure by formation of the contacts and a potentially denser material is obtained. However, the development of particle contact does not necessarily lead to denser material in the initial stage of sintering if matter is only transferred to the contact area from other parts of the particle surface. Surface energy term changes as the nature of the surface changes from solid-vapour to solid-solid contact. Both coarsening and densification can proceed simultaneously to form bonds and coarsen particles. A special case occurs when densification is followed by grain growth if sufficient energy is supplied. The relationship between pore size, grain size and theoretical density can be measured using the phenomena described. Avoiding coarsening before sintering should be the objective.

5.4 Stages of sintering

Sintering is a temperature and time-dependent phenomenon that results in densification. Sintering kinetics and the atomic mechanisms of mass transport vary during the different stages of sintering. Sintering can be divided into three stages based on pore shape and size.

Initial stage: Contact area between particles increases by neck growth.

Intermediate stage: Relative density increases, and pores become continuous in nature; this is the longest stage of sintering.

Final stage: Continuous pores become isolated pores.

The mechanisms of mass transport during solid-state sintering are as follows: evaporation and condensation, diffusion, and viscous flow (creep). These mechanisms are described below.

5.4.1 Evaporation and condensation

The driving force is the difference in vapour pressure between convex and concave surfaces, as shown in Figure 6. Two spherical particles of the same size are in contact when a conglomeration of particles is compacted. As such, two surfaces are created: at the point of contact there is a small concave surface, and away from the point of contact there is a convex surface. The difference in vapour pressure between the surfaces creates a vapour pressure gradient. More vapour pressure is present on a convex surface than a concave surface, so more material evaporates from the convex surface, is transported to the concave surface, and is condensed. This is because of the curvature rather than the temperature gradient. As more material evaporates and condenses in the concave area, the neck area increases, and the concave region becomes flatter. During this process, the distance between the centres of neighbouring particles does not change, which means that the overall dimensions will not change either. In other words, no shrinkage or densification is observed. An equation can be written for the evaporation and condensation mechanism to predict the rate of neck growth, which is initially very high and then slows down (time dependency). Neck growth decreases with increasing particle size (size dependency) and increases with an increase in the vapour pressure of the solid.

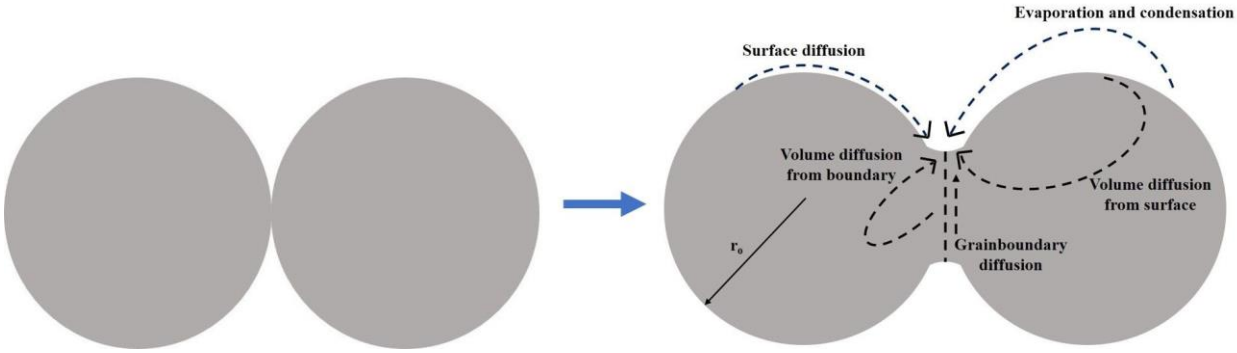

Figure 6: Schematic of different sintering mechanisms (redrawn from [97]*).*

5.4.2 Vacancy mechanisms of solid-state sintering

Thus, vacancy movement is driven from a concave surface to a convex surface. As seen in Figure 6, vacancy moves from concave to convex surfaces so that the flow of material goes in the opposite direction and the void fills. The movement of vacancies can take place along three different paths.

Lattice/volume diffusion: Vacancies which are generated in the concave surface are moved to a convex surface through the lattice or bulk of the material.

Surface diffusion: Vacancies move along the surface or close to the surface.

Grain boundary diffusion: Vacancies move from concave to convex surfaces as well as to flat surfaces, which are the grain boundary between adjacent particles.

Pipe diffusion: The green compacts in powder metallurgy (PM), when pressed uniaxially, are anisotropic porous structures with inhomogeneous plastic deformation at the inter-particle contacts give raise to large strains [98]. These dislocations have an effect on bulk diffusivity where the dislocation density is directly proportional to the bulk diffusivity [99]. Molinari et al. [100] estimated the dislocation density in the inter particle region and found that the density was comparable to those typical of heavily cold worked metals. Torresani et al. [98] proposed a micromechanical model for the shrinkage anisotropy during sintering of metal powder based on the mechanism of grain boundary diffusion and extended to take into account the dislocation pipe-enhanced volume diffusion.

The rate at which the above-mentioned diffusion occurs varies according to the given mechanism. The vacancy mechanism, unlike evaporation and condensation, results in shrinkage or changes in dimension, except in the case of surface diffusion.

The activation energy required for surface diffusion is the lowest among the three diffusion paths, followed by grain boundary and then lattice diffusion. Accordingly, surface diffusion is dominant at lower temperatures, while lattice diffusion dominates at higher temperatures. For smaller particle sizes, surface and grain boundary diffusion are the preferred diffusion paths.

There is not always a driving force to shrink the size of the pore during sintering. Under certain conditions, pores become thermodynamically stable. Pores become entrapped within the particles/grains, making it difficult to achieve theoretical density within a finite time. During the final stage of sintering, grain coarsening occurs along with pore elimination as average grain size increases with time. Larger grains grow at the expense of smaller ones. Hence, in practice, shrinkage during solid-state sintering requires a fine powder size; for this reason, normal water-atomized or sponge iron

powder, which has a median size in the range of 50–100 μm, shows very little (if any) shrinkage during sintering. The irregular shape of the powder also makes the sintering highly localized so that extensive shape accommodation is required to complete the sintering towards significant shrinkage. To this should be added that metal powder after compaction can be viewed as a highly deformed structure with significant increase of deformation structure, in particular at surface regions of the metal particles [101].

5.5 Sintering of micrometre-sized powder

During powder compaction, contact points between particles are mostly at iron oxide rather than the stable oxide as the majority of particle surfaces are covered by a thin iron-rich oxide layer. Ferrous powder has good sinterability as the surface oxide is easily reducible [102]. Efficient reduction of the iron oxide layer is important as the onset of the formation of inter-particle necks depends on reduction. Changes in surface chemical characteristics of ferrous powder and the formation of inter-particle connections occur during the heating stage, but there is also a risk of surface oxide enclosure inside the necks [7].

5.6 Nanopowder sintering

To improve the density of water-atomized iron powder and expand the application spectrum, nanopowder can be used as a sintering additive. During the sintering of a mixed powder composed of micrometre-sized powder and nanopowder, nanopowder could either show liquid-like sintering behaviour [103] or sinter at low temperatures and contribute to densification [5].

Nanoscale materials are valuable due to their modified solid-state properties [103]. One of the most interesting aspects of nanopowder is the melting point's dependence on particle size [104]. An early thermodynamic model was developed in 1909 to predict the melting-point depression of nanomaterials, and it was found that melting point temperature varied inversely with particle size [105]. Subsequent research has studied variations in melting temperature in relation to the particle size of metals like gold, silver, tin, indium, lead and aluminium [73]. Techniques like transmission electron microscopy, and calorimetry have been used to investigate melting-point depression [106]. This dependency is more prominent in the lower end of the size regime in comparison to large sizes [107]. Still, to take advantage of this effect to impose liquid phase formation only by size requires as illustrated in Figure 4, nanopowder size of typically 10-20 nm or smaller.

Ultrafine particles like nanopowder that have a diameter in the order of tens of nanometres have been of longstanding research interest. This interest could be

attributed to the unique physical and chemical properties associated with nanopowder in its ultra-dispersed state [108]. Sintering is a means of preparing bulk materials using nanopowder. According to the Turnbull classification of metastability, nanopowder has a metastable nature in terms of morphological metastability. The other ones are compositional, which is associated with extended solution ranges, and structural or topological, which are associated with a crystal structure or phases [109]. Nanopowder exhibits isotropic shrinkage and possesses low activation energy for sintering, and decreasing the sintering temperature is thus a representative advantage of nanopowder [110] [111]. Some additional challenges of nanopowder compared to regular micrometre-sized powder are particle agglomeration, inherent contamination, enhanced chemical reactivity, grain coarsening and loss of nano characteristics. The sintering mechanism of nanopowder may or may not be the same as that of regular powder. Additional drawbacks of nanopowder are high cost and low formability. An effective solution to these issues is to use a combination of nanometre- and micrometre-sized powder. One significant advantage of the addition of nanopowder in such cases is activated sintering by nanopowder [113].

The sintering of micro/nanopowder bimodal powder mixture has been studied in relation to metal injection moulding (MIM). MIM is an attractive, cost-effective mass production technology that combines injection moulding and PM to manufacture net-shaped complex components [114]. In the aforementioned study, densification of the micro-nanopowder mixture started below 800 °C and decreased with the increasing proportion of nanopowder in the mixture [113] due to the lower sintering activation energy attributed to the excess surface energy of the nanopowder [111]. The relative sintered density of the micro-nanopowder compact was higher than that of the micrometre-sized powder compact alone [113]. There is a significant difference between the relative sintered density of the micro/nanopowder bimodal powder compact and the micrometre-sized powder compact in relatively low temperature ranges (1000 °C); this difference occurs because of the denser grain boundary caused by sintered nanopowder around the micrometre-sized powder, which provide many diffusion paths and compact density is increased [5]. Joon et al. observed that the relative sintered density increased from 73% to 90 % between the temperature range of 800-900 °C in a micro/nanopowder bimodal powder MIM compact [5]. Similar behaviour was observed in press and sintered 316L stainless steel micro-nanopowder bimodal powder compacts [115].

5.7 Mixing of powder

Powder mixing is of the utmost importance in the PM industry to ensure the repeatability of properties. The main challenge of powder mixing is the mixing and

simultaneous deagglomeration of fine particles that naturally tend to agglomerate. However, high chemical reactivity and attraction due to surface energy make them attractive to use [116]. High energy and force are applied to break down agglomerates and mix them. Ball milling is performed to grind fine powder, and ball size and ratio are chosen according to the material to be ground [117]. In alumina and zirconia systems, bimodal ball size distribution helps simultaneous deagglomeration and mixing [117]. While deagglomeration and mixing is prime concern of the present doctoral study, using ball was not pursued owing to the risk of affecting powder shape too much. Instead, a mild approach was applied for powder mixing of the micro/nano bimodal powder mixes studied as outlined below in Chapter 6 Materials and Methods.

CHAPTER 6

MATERIALS AND METHODS

The main objective of this thesis is to improve the density of sintered compacts through the addition of nanopowder to water-atomized powder. For this purpose, water-atomized iron and steel powder served as base powder to which nanopowder was added. The bimodal powder was subjected to compaction and sintering. Nanopowder was characterised by its surface constituents using X-ray photoelectron spectroscopy and Auger electron spectroscopy. To understand the reduction mechanism for nanopowder alone, thermogravimetry was also employed. Nanopowder was further characterised using scanning electron microscopy and transmission electron microscopy. Sintering studies were performed with a dilatometer that allowed for precise control of both shrinkage and atmospheres.

6.1 Materials

6.1.1 Base powder

The base material in the present study was water-atomized iron and steel powder grades, both produced by Höganäs AB, Sweden. The water-atomised iron powder was commercially available powder grade with a trade name ASC 300. Chromium-pre-alloyed steel powder admixed with nickel and carbon with the designation CrA+Ni+C was used as the base water-atomized steel powder mix. CrA is chromium pre-alloyed steel powder, and CrA+Ni is this powder admixed with nickel. Carbonyl powder, commercially procured from BASF, is produced through thermochemical decomposition process and was also used as a base powder for comparative studies. This powder was finer in size compared to the ASC 300 or CrA+Ni with d_{50} of ~5 μm. The compositions of these water-atomized powder grades are listed in Table 2.

Table 2: Composition of ASC 300(-45 μm) and CrA+Ni powder

Elements	C	O	Cr	S	Ni	Fe
ASC 300, wt.%	0.005	0.114	0.056	0.0093	-	Rest
CrA+Ni, wt.%	0.01	0.155	1.8	0.002	2.0	Rest

The ASC 300 was sieved to <45 μm and used in this size class, whereas CrA+Ni had a size distribution of 20 to 180 μm. The CrA and CrA+Ni powder variants of size fractions of -45 and 20-180 μm were also used. The particle size distribution for ASC 300 is shown in Figure 7.

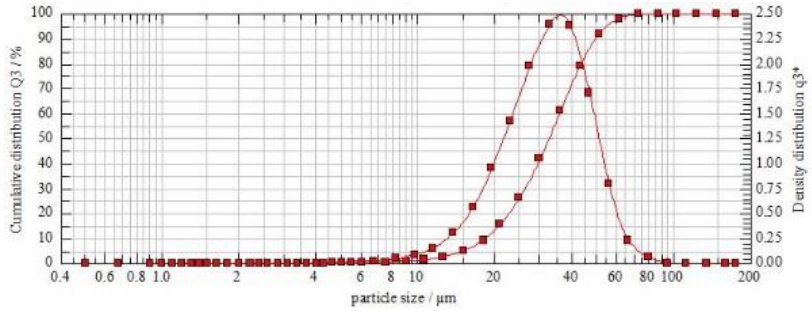

Figure 7: Particle size distribution of ASC 300 (-45 µm) water-atomized iron powder.

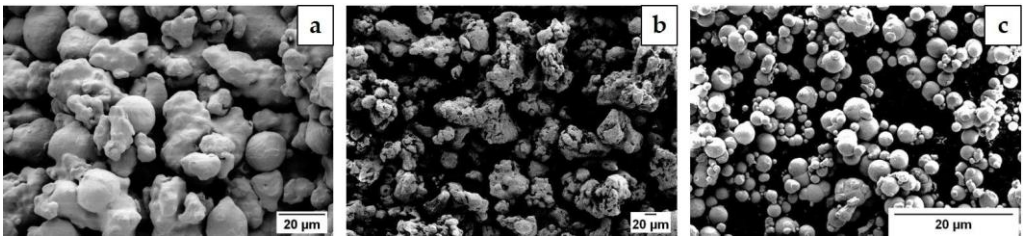

Figure 8: Scanning electron micrographs showing the morphology of the base powder (a) ASC 300, (b) CrA+Ni+C and (c) carbonyl powder.

Figure 8a-b illustrates the irregular morphology of the water-atomized powder variants, a signature of the water atomization process, whereas Figure 8c shows the spherical morphology of carbonyl powder. For these kinds of powder grades, the oxygen present in the powder is mostly bound in the form of an iron-rich oxide film covering the majority of the powder surfaces. Oxygen is also bound to a minor extent in particulates surface oxides rich in elements like chromium and manganese [7]. The thickness of the iron-rich oxide film for plain iron and chromium pre-alloyed grades was in the range of 5-7 nm [118] [119] [118] [120]. The iron-rich oxide layer's composition depends on the composition of the powder [7].

6.1.2 Nanopowder

Four different kinds of nanopowder were explored as sintering aid in this thesis study. Pure iron nanopowder, used for the majority of the experiments in this thesis study, was procured from Sigma Aldrich (Fe NP). Three different size fractions were used, namely 35-45, 40-60 and 60-80 nm, all below 100 nm, were used. Steel nanopowder (steel NP) was produced through an in-house technology, developed in the Department of Microtechnology and Nanoscience, Chalmers University of Technology by Professor Liu and colleagues. The composition of the steel rod used to produce nanopowder is listed in Table 3. The size of the steel nanopowder ranged from a few nanometres to a submicron. Both iron and steel nanopowder were covered by an oxide scale, though the steel nanopowder scale was thicker than that of the pure iron nanopowder; this was attributed to the exposure of steel nanopowder to water

during the production process. Further information on this is found in Chapter 7 Summary of Results and in Paper I.

Table 3: Composition of the steel rod used to produce the nanopowder

Elements	C	Mn	Si	S	P	Fe
wt.%	0.16-0.24	1.30-1.60	0.10-0.40	0.06 max	0.06 max	Rest

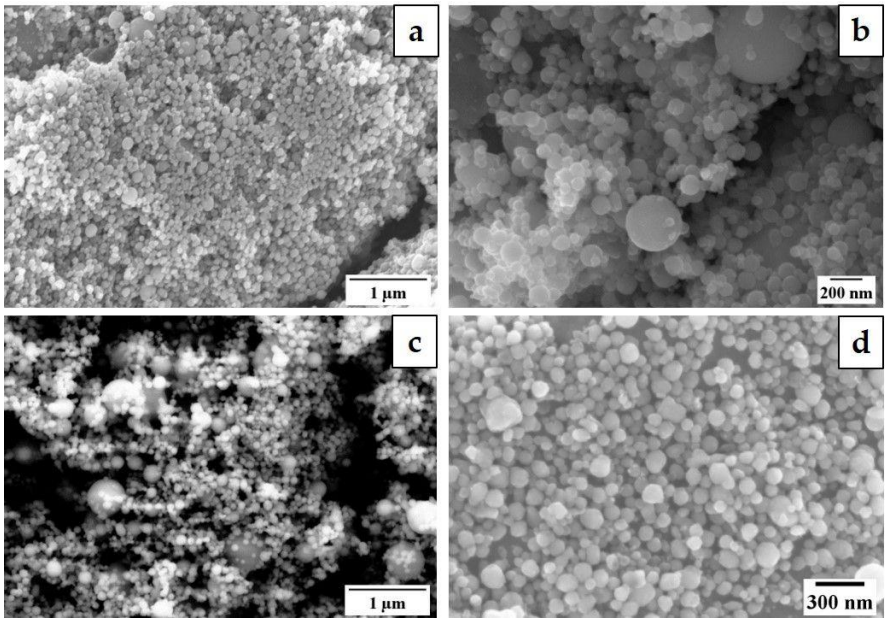

Figure 9: Scanning electron micrographs showing the morphology of the different nanopowder (a) iron nanopowder, Fe NP, (b) steel nanopowder, steel NP, (c) carbon containing nanopowder, CP NP and (d) carbon-coated nanopowder, CC NP.

Table 4: Carbon and oxygen content of different nanopowder

Nanopowder	Carbon, wt. %	Oxygen, wt. %
Fe NP	0.05	5.5
CP NP	0.1	3.1
CC NP	4.70	7.5

Two different kinds of iron nanopowder variants coated with carbon were also used as sintering aids. The first variant of carbon-coated nanopowder, was procured from Sigma Aldrich and less than 50 nm in size (CC NP). The second variant of carbon-coated nanopowder was procured from Nanographene (CP NP). The size of this powder was less than 100 nm, but the powder had a few agglomerates. Iron oxide

nanopowder was procured from Sigma-Aldrich, which was used as a reference in Paper III. Figure 9 shows the electron micrographs of the different nanopowder variants. The carbon and oxygen values of Fe NP, CP NP and CC NP are given in Table 4.

All nanopowder variants were supplied in the dry state. Commercial nanopowder was supplied by the manufacturer in sealed bottles. Storing and handling of the powder were carried out using a nitrogen filled glove box. The box was also used in sample preparation for different characterisation techniques. Samples were transferred from the glove box to different equipment with the utmost care. On exposure to the atmosphere, no nanopowder showed any signs of explosive oxidation. The different powder designations are given in Table 5.

Table 5: Details of different powder used and their designation

Powder	Designation
Water-atomized iron powder	ASC 300
Water-atomized steel powder (pre-alloyed with 1.8 wt.% Cr)	CrA
Water-atomized steel powder admixed with 2 wt.% Ni	CrA+Ni
Water-atomized steel powder admixed with 2 wt.% Ni and 0.3 wt.% C	CrA+Ni+C
Iron nanopowder	Fe NP
Steel nanopowder	Steel NP
Carbon coated nanopowder (from Nanographene)	CP NP
Carbon coated nanopowder (from Sigma Aldrich)	CC NP

6.1.3 Mixing of the powder/powder blend

Mixing of micrometre-sized powder and nanopowder was carried out in a tumbler placed in the glove box to yield variants of the bimodal powder mixes. In Paper IV, ASC 300 was combined with 5 wt.% iron nanopowder and steel nanopowder. Carbon in the form of graphite was also added to some of the powder blends to study the influence of the addition of carbon on sintering. Other sets of powder blends were made by varying the amount of nanopowder content. In Paper V, carbonyl iron and ASC 300 powder were mixed with iron nanopowder in different proportions of 5, 25,

50 and 75 wt.%. In Paper VI, ASC 300 powder was mixed with 5 wt.% iron nanopowder coated with carbon. In Paper VII, CrA and CrA+Ni grades of different size fractions were combined with 5 wt.% iron nanopowder. Papers VIII and IX used a CrA+Ni+C mix combined with 5 wt.% iron nanopowder.

6.1.4 Choice of nanopowder

This doctoral thesis is an initiating study to evaluate the idea of utilising nanopowder as a sintering aid in press and sinter powder metallurgy (PM) steel. The initial aim was to minimise the impact of alloying composition by means of master alloy approach on overall composition. Additionally, the thesis verifies if melting occurs with these additives under a range of sintering temperatures.

Iron nanopowder and carbon-coated nanopowder are commercially available. The steel nanopowder was produced and supplied by means of a technique that provides substantially higher production rates compared to standard production methods [6]. The quality of the powder produced and its applicability as a sintering aid were assessed. Apart from carbon's role as a reducing agent and as alloying element, carbon-coating (also paired with different types of graphite) was used to evaluate the possibility of modifying the temperatures at which densification can be achieved as well as to explore if carbon-coating can constitute a carbon source in addition or instead of the normal added graphite. Carbon-coating, while expected to hinder the initial surface oxide reduction by hydrogen, can also contribute to more efficient carbothermal reduction at higher temperatures when carbon becomes active.

One of the major challenges in the addition of a master alloy to press and sinter steel is obtaining uniform distribution in compacts. Uneven distribution of the alloying elements contributes to non-uniform microstructures and properties with quality issues. The chosen sintering aids do not substantially modify the composition of the steel in negative manner.

6.1.5 Compaction and delubrication

In most of the experiments in this thesis study, bimodal powder mixtures were compacted using an in-house compaction press in the Department of Industrial and Materials Science, Chalmers University of Technology under uniaxial loading conditions without the addition of lubricant. Varying compaction pressures ranging from 300 to 700 MPa were applied. The diameter of compacts was 10 mm, and height varied from 1.5 to 4.5 mm depending on the amount of nanopowder and the compaction pressure employed. In Paper IV, the compacts containing 5 wt.% nanopowder were mixed with 0.6 wt.% Lube-E for lubrication and compacted by Höganäs AB. Compaction pressures of 400, 600 and 800 MPa were then employed. Cylindrical samples of 13.5 to 14.5 mm in height and 11.5 mm in diameter were then

produced from the powder blends. In Paper IX, Charpy impact bars of CrA+Ni+C and CrA+Ni+C+Fe NP were uniaxially compacted at Höganäs AB to same green density. Lubricant, 0.6 wt.% Lube-E, was used and a compaction press of 600 and 1100 MPa was used for CrA+Ni+C and CrA+Ni+C+Fe NP, respectively to achieve the same green density.

For the compacts with lubricant, delubrication of compacts was performed at 450 °C in a pure argon (99.999%) atmosphere at a flow rate of 4 l/min to minimise oxidation. There may have been some oxygen pick up during this operation, but the subsequent sintering was performed in a pure hydrogen environment. A heating rate of 10 °C/min was used to reach the target temperature and this temperature was held for 30/60 min and then cooling was done.

6.2 Methods

Several analytical methods were used, including surface analytical techniques, thermoanalytical techniques, microscopy, and hardness/impact testing. Surface analytical techniques involved characterising the surface chemical characteristics of samples. Thermoanalytical techniques involved continuous monitoring of chemical and physical (dimensional) changes in samples as a function of temperature and time under controlled experimental conditions. Microscopy (optical and electron) was used for evaluating the microstructure and morphology of the materials being studied. Impact strength and hardness were measured for selected sintered materials to assess mechanical properties.

6.2.1 Thermogravimetry

Thermogravimetric analysis (TGA) is a technique in which the change in mass, Δm, of a sample is measured as a function of temperature and time in a specified atmosphere [121]. The rate of mass change is measured as the first derivative of the mass change curve, $\Delta m/dt$. In TGA, the sample is heated according to the pre-set temperature profile in a controlled atmosphere, and the change in mass is recorded. Mass can be gained or lost, depending on the reaction of the sample to the specified atmosphere as the temperature increases. The TGA can be used to evaluate oxidation, reduction, decarburisation, decomposition, and so on, during the heating operation for industrial applications. Along with variety of atmospheres like inert, oxidising and reducing, vacuum can also be employed for numerous experiments. The mass of the sample is measured before the analysis, and the relative mass change is recorded during TGA. The required equipment consists of a sample holder, furnace, vacuum system, high-resolution balance, and thermocouple. The setup is vacuum-tight to provide good atmosphere control during the experiment.

This study used a Simultaneous Thermal Analyser STA 449 F1 Jupiter (NETZSCH Thermal Analysis GmbH, Germany), which is a high-sensitivity balance system with a resolution of 25 ng. It is a top-loading system with an ultra-nano balance. To measure the temperature, a W/Re thermocouple was used. An alumina crucible was used as a sample carrier for all the TGA experiments. The sample to be analysed was filled in the alumina crucible inside the glove box and transferred to the STA. The mass of the crucible and the sample were measured before the start of the experiment. After loading the sample, the system was evacuated and purged with argon three time before the start of experiment; this was done to reduce air residue and ensure that the atmosphere was good enough for the use of hydrogen during the experiment. Scientific grade hydrogen of 99.9999% purity was used for all the TGA experiments. A flow rate of 100 ml/min was maintained throughout the experiments. Schematic of STA and TG graph showing the mass change in Fe NP are seen in Figure 10.

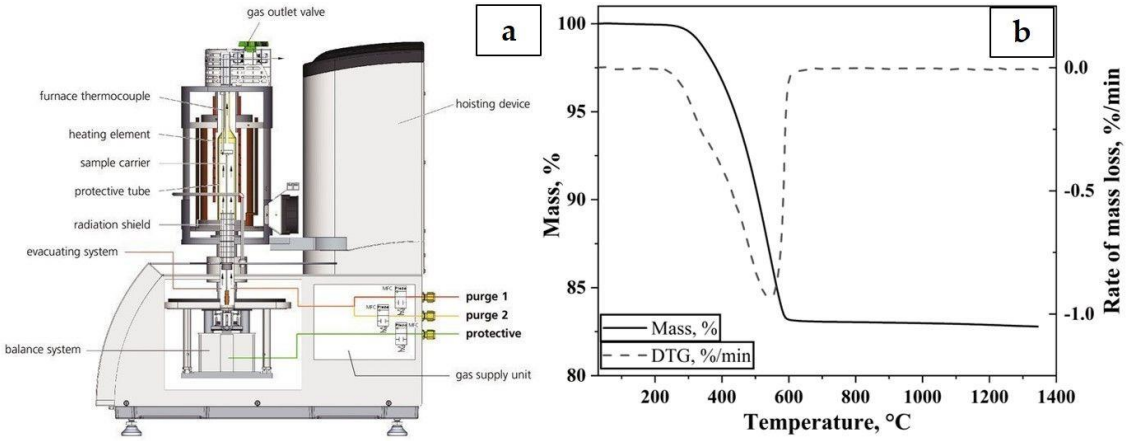

Figure 10: (a) Schematic of the simultaneous thermal analyser STA 449 F1 Jupiter from Netzsch (with permission from NETZSCH-Gerätebau, Selb, Germany), (b) thermogravimetry graph showing the mass loss and rate of mass loss as a function of temperature. Iron nanopowder was heated to 1350 °C at 10 °C/min in pure hydrogen.

Different temperature programmes ranging from 400-1350 °C with varying heating rates were used to analyse both bimodal powder mixtures and nanopowder alone. In Paper I, pure iron nanopowder of different sizes was subjected to heating up to target temperature of 1350 °C at a heating rate of 10 °C/min. These results helped in understanding the surface oxide layer reduction of pure iron nanopowder. To study reduction kinetics, in Paper III involved pure iron nanopowder and iron oxide nanopowder being heated to 1350 °C at different heating rates of 5, 7, 10, 20, 25, 30, 40 and 50 °C/min. For Paper VI, mass change behaviour with respect to use of carbon-coated nanopowder was evaluated for heating to 1250 °C. Paper VII evaluated the influence of nanopowder addition to CrA and CrA+Ni using TGA. A heating rate of 10 °C/min was then used to reach the peak temperature of 1250 °C. A similar exercise

was done in Paper IX in which CrA+Ni+C with and without nanopowder was analysed for mass change. Detailed experimental descriptions can be found in the different appended papers. A sample mass of 500 mg was used for nanopowder whereas a mass of 2 g was used for bimodal powder mixtures.

6.2.2 Differential scanning calorimetry

A calorimeter is used to measure the heat released or absorbed by a sample under a controlled temperature program. Differential scanning calorimetry (DSC) is a thermoanalytical technique used for measuring the amount of energy absorbed or released by a sample when it is subjected to heating or cooling. As the name suggests, the amount of energy absorbed or released is measured with respect to a reference. Heat is supplied to the sample and reference, and the corresponding change in temperature is recorded using the sample's radiated or absorbed heat. In a simple DSC setup, energy is introduced into the sample and the reference, meaning that temperature is uniformly raised over the timeframe. The sample absorbs or releases energy depending on the endothermic or exothermic processes it undergoes. The DSC technique is useful in evaluating endothermic and exothermic processes like melting temperature, heat of fusion, reaction enthalpy and temperature, glass transition temperature, phase transition temperature, specific heat, or heat capacity, and so on.

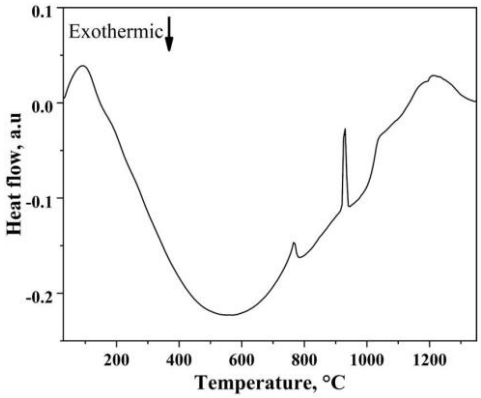

Figure 11: Differential scanning calorimetry curve of iron nanopowder showing endothermic transformations, such as Curie temperature at 768 °C and alpha to gamma phase transition at 910 °C, when heating to 1350 °C in an argon atmosphere.

There are two types of DSCs depending on operation mechanism: heat flux DSC and power-compensated DSC. In a heat flux DSC, the sample pan and reference pan are placed inside a furnace which is heated at a pre-set heating rate, and heat is transferred to the pans through a thermoelectric desk. In a power-compensated DSC, the sample and reference are placed in separate furnaces heated by separate heaters. The sample and reference are maintained at the same temperature, and the difference in the thermal energy required to maintain them at the same temperature is measured. A

variety of crucibles like aluminium, copper, platinum and alumina are available, and one is chosen depending on the material and temperature being analysed. Different gases like nitrogen, air, oxygen, and argon can be used in the process atmosphere.

This thesis study used a simultaneous thermal analyser STA449 Jupiter F9 (NETZSCH Thermal Analysis GmbH, Germany) with a combined TG/DSC sensor and an S-type thermocouple. An alumina crucible and argon atmosphere were used for all the analyses. The sample, generally in the range of 100-250 mg, was loaded in the small alumina crucible and placed in the crucible tray along with the reference crucible. The experiments were run in a high-purity argon atmosphere (99.9999%) at a heating rate of 10 °C/min. The DSC experiments were carried out at 1450 °C to measure the phase transitions and melting temperatures of different nanopowder, if any. Figure 11 illustrates results from a DSC run on iron nanopowder.

6.2.3 Dilatometry

Dilatometry is a thermoanalytical technique used to characterise dimensional changes in a material as a function of temperature by means of measuring axial shrinkage or expansion in relation to temperature and time. Dilatometry is also used for performing rate-controlled sintering studies on PM compacts and the thermal expansion in materials. Data is generated in the form of dimensional change against time and temperature [122]. A push-rod dilatometer is used for thermal expansion measurements and sintering studies of PM compacts. To perform the analysis in this thesis study, the sample was placed in the sample holder region and the push rod was positioned directly on the specimen. This pushrod, which is a frictionless sensing rod in the centre of a furnace tube, transmitted the dimensional change during the temperature changes. A linear variable displacement transducer was used as a sensing element for length changes. A thermocouple was placed close to the sample to control the temperature programme.

In the present study, the horizontal pushrod dilatometer DIL402C (NETZSCH Thermal Analysis GmbH, Germany), equipped with a vacuum furnace, was used (Figure 12a). The results obtained for iron powder compact heated to 1350 °C in pure hydrogen are illustrated in Figure 12b. A W-Re thermocouple was placed in the centre of the furnace alongside the pushrod. The sample was placed perpendicular to the pushrod, which was positioned against the sample using a weak force (30 cN). During the experiment, the linear displacement of the pushrod was converted into a measurement. As in the TGA experiment, the dilatometer was evacuated and purged with argon (99.9999% purity) three times before the commencement of the sintering experiment to ensure that the atmosphere was free of contaminants. For the majority

of experiments in this study, a high-purity hydrogen atmosphere was used, and for the reminder of the experiments a 90%N_2-10%H_2 atmosphere was used.

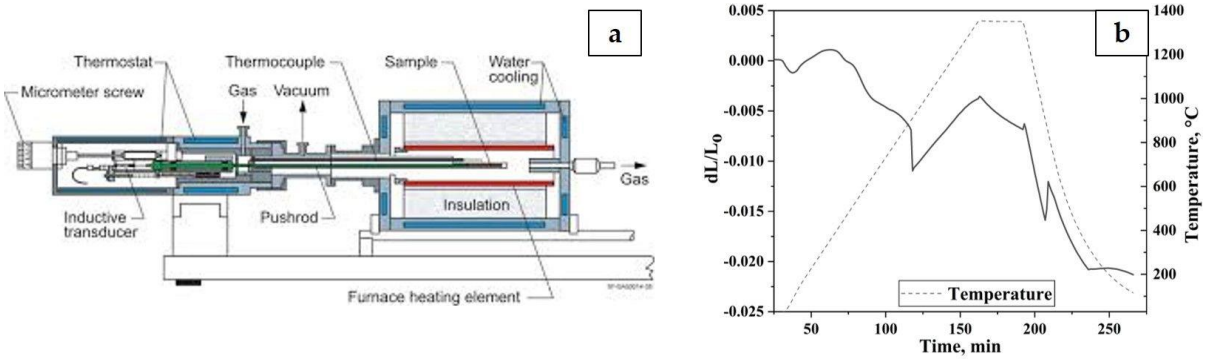

Figure 12: (a) schematic of the DIL402C dilatometer from Netzsch (with permission from NETZSCH-Gerätebau, Selb, Germany), (b) sintering curve taken from dilatometer showing the dimensional change undergone by iron powder compact as a function of temperature and time. Iron powder compact was heated to 1350 °C at 10 °C/min in pure hydrogen.

In this thesis study, most of the experiments were run to final temperature of either 1250 °C or 1350 °C. In Paper IV, the samples were sintered at different temperatures ranging from 500 °C to 1350 °C. In addition, different heating rates were employed, such as 5, 10 and 30 °C/min. In Paper V, sintering was carried out at final temperature of 1350 °C, with a holding time of 60 minutes at this peak temperature. Different heating rates like 2, 5 and 10 °C/min were employed. Paper VI carried out sintering at 1250 °C. In Paper VII, sintering was carried out at 1250 °C and 1350 °C. In Paper VIII, sintering was carried out at 1250 °C. Finally, in Paper IX, sintering was carried out at 1250 °C and 1350 °C. Experimental details are provided in the respective appended papers.

These thermoanalytical techniques yield information about the physical and chemical changes for the sample as a function of temperature and time.

6.2.4 X-ray photoelectron spectroscopy

X-ray photoelectron spectroscopy (XPS) is a surface-sensitive technique widely used for surface chemical analysis that provides both quantitative and chemical state information and that can be applied to a broad range of materials. It is also known as electron spectroscopy for chemical analysis (ESCA). XPS is based on the principle that a surface is irradiated by X-rays and emits photoelectrons due to the photoelectric effect [123]. Soft X-rays with specific energies are used for irradiating the sample and to generate photoelectrons. Typically, mono-energetic Al Kα radiation is used. The analysis is carried out in an ultra-high vacuum setup. When a photoelectron is ejected from a core level, this electron will attain kinetic energy given by the kinetic energy of the X-ray and the binding energy of the electron in question. The kinetic energy of the

emitted photoelectron can then be analysed using a hemispherical analyser. The characteristic binding energy (***BE***) of the photoelectron is given by the expression as follows:

$$\boldsymbol{BE = h\vartheta - KE - \phi} \quad \textbf{(2)}$$

where $h\vartheta$ is the energy of the exciting X-ray radiation, KE is the measured energy of the emitted electron from the solid and ϕ refers to the work-function for the specific instrument and material. As said, The BE is unique of each electron level for each element. The binding energy and intensity of a photoelectron peak give information about the elemental identity, chemical state and quantity of the element [124].

One of the important capabilities of XPS is its ability to measure the shift in core electron binding energy, which results from alterations in the chemical environment, that can be due to changes in the nearest neighbour, oxidation state or compound characteristics. These photoelectrons possess relatively low kinetic energy and have a higher probability of undergoing inelastic collisions with atoms if they travel far before leaving the surface. The electrons originating from a few atomic layers below the surface are used for analysis, making XPS a surface-sensitive technique. Typical analysis depth is 3 to 5 nm, depending on the density of the material. Consequently, the experimental setup requires an ultra-high vacuum environment, $<10^{-9}$ mbar. Depending on the number of elements present, electron attenuation length and the number of electrons are proportionally detected. The detection limit for the elements depends on the atomic number, but can be typically measured in the range of 0.1 to 1 at.% [125].

Two XPS instruments were used in this study. Paper I used the PHI 5500 instrument (Physical Electronics, Chanhassen, Minnesota, USA). This instrument is equipped with a monochromatic Al Kα (1486.6 eV, photon energy) X-ray source. Ultra-high vacuum conditions of 10^{-9} mbar were maintained during the powder analysis. The spectrometer and the X-ray source formed an angle of 90° with one another, creating a 45° angle with the sample surface. For the survey scan, the pass energy employed was 93.9 eV and 0.4 eV/step were used, and a high-resolution XPS was performed for elements of interest using 23.5 eV pass energy and 0.1 eV/step. The high-resolution XPS (HR XPS) provided oxide and metal peaks to evaluate shell oxide thickness. Before the measurements, energy calibration was carried out using the pure elemental standards of gold, silver, and copper. The etching was performed using argon gas with an accelerating voltage of 4 kV. A raster scan via an argon ion beam over an area of 4 x 5 mm^2 to 2 x 3 mm^2 gave an etch rate of 3 to 5 nm/min. The etch rate was

calibrated on flat Ta foils with known Ta_2O_5 thickness (100 nm), and thus the oxide thickness was expected to be of the same magnitude as that of iron-oxide [126].

For Papers II, III and VI, the PHI VersaProbe III instrument was used, which was also equipped with a monochromatic Al Kα (1486.6 eV, photon energy) X-ray source. Further details about the analyses are found in the appended papers.

Nanopowder was mainly analysed for surface characteristics using XPS. Samples for XPS analysis were prepared inside the glove box. Two kinds of sample preparation methods were adopted. In the first method, the nanopowder was mounted on a double-sided adhesive conductive carbon tape, while in the second method powder was lightly pressed onto aluminium plates. For sintered compacts, double-sided adhesive conductive carbon tape was used. To analyse and curve-fit the data, PHI MultiPak (v.9.7.0.1) was used. Iterated Shirley background correction was applied to remove the peaks from an inelastic scattering background and asymmetric components were assigned for area integration.

6.2.5 Auger electron spectroscopy

Auger electron spectroscopy (AES) is one of the most common surface analytical techniques. AES can be used for executing tasks such as determining the composition and thickness of coatings on powder [127]. Similar to XPS, AES uses the energy of emitted electrons to identify the elements present in the material. The main difference between these two techniques is the use of X-rays to eject an electron in XPS, whereas an electron beam is used for the same function in AES. The spatial resolution of AES is higher than that of XPS owing to the use of electron beam. Like XPS, AES is used for depth profiling as well as analysing powder systems [120] [128] [53] [129]. AES collects information from 1 to 5 nm from the surface of the sample. This limited depth is due to the small escape depth of Auger electrons, which means that only a few atomic layers can be analysed. The interaction volume is relatively small as the Auger signal is recorded for a small area of approximately 10-20 nm depending on electron beam setting. This high lateral resolution is a result of the use of field emission gun. AES measures the kinetic energy of an escaping Auger electron generated by the Auger process. Because a primary electron beam is directed onto the sample, a core electron can be ejected, creating a vacancy. This vacancy is filled by another electron from the outer principal shell, and this jump produces sufficient energy to eject an Auger electron from the outer principal shell.

As the electron beam is the primary source, an ultra-high vacuum system is used. Apart from the vacuum system, an electron source and a detector form important parts of AES. For this thesis, measurements were performed using a scanning PHI 700

instrument using an accelerating voltage of 10 kV and a beam current of 10 nA, which produced a lateral resolution of about 20 nm. These measurements were mainly used to evaluate the surface characteristics of nanopowder.

6.2.6 Chemical analysis

The bulk carbon and oxygen levels of both powder and sintered compacts were determined using LECO TC-600 and LECO CS-844 instruments. For oxygen analysis, the sample was placed in a graphite crucible and melted in an induction furnace under a flow of helium. The oxygen present in the sample reacted with the crucible, forming CO and CO_2. The CO and CO_2 amounts were measured by means of infrared (IR) sensors and used to estimate the amount of oxygen. To measure carbon, the sample was combusted in an induction furnace under the flow of oxygen. Based on the CO and CO_2 formed due to the reaction between carbon in the sample and oxygen, the amount of carbon in the sample was determined.

6.2.7 Scanning electron microscopy

Scanning electron microscopy (SEM) uses a focused beam of electrons to bombard the sample surface and interact with the sample, generating a variety of signals. The source for electrons in SEM emits high-energy electrons that are directed onto the specimen. These primary electrons carry significant amounts of kinetic energy, and when they hit the sample, they interact with the specimen and generate different signals (electrons and X-rays). This interaction volume between electrons and the specimen has a depth of up to between 1 to 5 μm. The different signals that are generated include secondary electrons, backscattered electrons, diffracted backscattered electrons, Auger electrons and photons. Secondary electrons are used for topographic imaging, while backscattered electrons are used to illustrate the contrasting compositions of multiphase samples. X-ray generation due to the inelastic collisions between the incident and sample electrons can be used to analyse the chemical composition of the sample via energy dispersive spectroscopy (EDS). The energy of the electron beam typically ranges from 1 to 40 kV. A typical SEM consists of an electron source, electromagnetic lenses to focus the electron beam on the specimen, sample stage, different detectors for the signals of interest, output devices and vacuum systems. There are various kinds of electron sources, such as tungsten filament, LaB_6 filament and field emission gun (FEG).

In the present study, the high-resolution scanning electron microscope (HR SEM) LEO Gemini 1550 (CARL ZEISS electron microscope GmbH, Germany) (FEG-SEM) equipped with an X-Max EDS detector was used for performing the microscopy analysis.

6.2.8 Electron backscattered diffraction

Electron backscattered diffraction (EBSD) is an SEM-based technique that provides information about crystal orientation, grain size, texture, phase identification, strain analysis and level of deformation. Primary electrons hit the sample, resulting in the production of scattered electrons in different directions (diffuse scattering). The diffracted electrons, which satisfy the Bragg's diffraction, generate diffraction cones that are detected on the phosphor screen of the EBSD detector, thereby giving rise to EBSD patterns. An SEM can be equipped with an EBSD detector for the acquisition of the patterns as well as software to process the data. The sample is placed at approximately 70° with respect to the electron beam.

In this thesis study, EBSD data were acquired using an HKL Nordlys EBSD detector (Oxford Instruments) installed on a LEO Gemini 1550 FEG-SEM. An accelerating voltage of 20 kV was applied at a working distance of 10-20 mm with a step size of 0.10 μm. The data acquired was processed using AZtecCrystal software and the open-source MATLAB MTEX toolbox.

6.2.9 Transmission electron microscopy

Similar to SEM, transmission electron microscopy (TEM), uses electrons as a source of imaging. The TEM is the most popular instrument in characterising nanomaterials. In TEM, a high-energy beam of electrons is transmitted through a very thin sample. Acceleration voltage can be anywhere between 100 kV to 1.5 MV depending on the equipment. The emission of electrons from the electron gun is done either by thermionic or field emission. The electrons from electron gun are focused into a small, thin, coherent beam. Part of the electrons passes through the sample and a part is diffracted. The transmitted portion is focused on the fluorescent screen to obtain a bright field image [130] [131]. In this thesis study, nanopowder was analysed using a high-resolution TEM (HRTEM, FEI Titan 80-300), and samples were prepared using a copper grid. Experimental details are given in Paper VI.

6.2.10 X-ray diffraction

X-ray diffraction (XRD) is generally used for phase identification in materials. It provides information on structures, phases, preferred crystal orientations (texture) and crystallinity. XRD peaks are produced by the constructive interference of a monochromatic beam of X-rays scattered at specific angles from each set of lattice planes in a sample [132]. Constructive interference occurs when Bragg's law is satisfied. In this study, a Bruker AXS D8 Advance diffractometer with Cr Kα radiation (λ=2.28970 Å) operated at 35 kV and 50 mA was used.

6.2.11 Optical microscopy

Light optical microscopy (LOM) is a basic yet powerful tool in the field of materials science. LOM uses light in the visible spectrum to image the topography or phase composition/feature contrast of a sample. LOM is mostly useful for features of sizes down to the micron range. Image resolution is limited by the wavelength of the light and the numerical aperture of the objective. The LOM works on the principle of reflection, wherein a light source is directed onto the surface of a sample and the reflected light is collected through the lenses, thus forming an image. The sample surface must be reflective in nature for LOM to function.

In this thesis, a Zeiss Axioscope 7 microscope equipped with a Zeiss digital camera 35 and AxioVision software for analysis was used. The samples of interest were mounted in a resin (Polyfast by Struers) using a hot mounting machine (Citopress-20, Struers). The mounted sample was subjected to grinding and polishing to render the sample surface mirror-like surface. The samples were then etched using 2 vol.% nital solution (2% HNO_3 in ethanol) to reveal the microstructure under LOM. A porosity analysis was carried out on an unetched sample surface using ImageJ freeware. Images were taken from 20 different locations per sample for the porosity analysis. Trainable Weka Segmentation tool, part of FIJI ImageJ freeware [133] [134], was used for the analysis phase fractions in Papers VI and VIII.

6.2.12 Hardness

Vickers hardness was measured using a Struers DuraScan-70 G5, under a load of 1 kg on metallographic cross-sections of sintered compacts. A minimum of 10 indents were performed per sample, and an average hardness value was documented.

6.2.13 Density measurement

Density measurements were carried out on green and sintered compacts to determine differences in density due to the sintering process. For the green compacts, density was evaluated by measuring the mass and volume of the sample using a simple balance of 0.0001 g accuracy and conventional measuring tools. Green density was also measured using LOM. The Archimedes principle (ISO 3369) was used to measure the density of sintered samples; for this, the mass of the sample was measured in air and in water with sealed pores when required.

6.2.14 Impact testing

Impact testing was performed on impact energy (IE) bars prepared according to ISO 5754 to evaluate the IE values. The CrA+Ni+C and CrA+Ni+C+Fe NP powder were compacted to the same density and subsequently sintered at 1250 °C. The sintered IE

bars were tested, 3 samples per condition, using Instron Charpy 450 MP2J2 impact tester, and the energy values were noted.

6.2.15 Design of experiments

Design of experiments (DOE) was used to identify the most pertinent factors that affect sinter density and the hardness of the powder compacts. A full factorial design was considered the most reliable approach based on a mathematical model of the combined effects of the processing factors [135]. Four factors chosen that were determined to be pertinent (Table 6) were categorical in nature. JMP 7 software (from the SAS Institute, Cary, NC, USA) was applied to analyse the results. DOE was used to design the experiments based on the list in Table 6.

Table 6: Experimental conditions of two-level factorial design

Factor/variables	Levels	
	-1	+1
Sintering temperature, °C	1250	1350
Particle size, μm	<45	SF (20-180 μm)
Iron nanopowder (Fe NP)	Without Fe NP	With Fe NP
Composition	Without Ni	With Ni

6.2.16 JMatPro

JMatPro 10.2 in conjunction with general steel database was used to depict the phase fractions of the investigated alloys.

CHAPTER 7

SUMMARY OF RESULTS

This chapter offers a synopsis and synthesis of the results obtained within the framework of this thesis. The appended papers and this chapter detail the work done throughout the thesis. The results are categorised into three different sections. The first section broadly addresses the characterisation of the nanopowder in terms of surface chemicals and thermal analyses. The second section deals with mixing nanopowder with water-atomized iron powder and the subsequent evaluation of compaction and sintering, with particular reference to sintering mechanisms. The third section addresses the fundamental role of nanopowder as an aid in the sintering of water-atomized iron powder. Investigations were performed to reveal the influence nanopowder's addition has on compaction and sintering when using water-atomized steel powder as a base powder. Papers related to each section are specified in the caption for each sub-title.

7.1 Characterisation of nanopowder (Papers I, II and III)

Since surface oxide reduction is a prerequisite for the progress of sintering, the first two research questions were formulated to address surface oxide reduction in the context of nanopowder when employed as a sintering aid. This section discusses the characterisation of nanopowder in relation to surface oxides and their reduction.

Various kinds of iron-based nanopowder iron (Fe NP), steel (steel NP), carbon-coated from Nanographene (CP NP) and carbon-coated from Sigma Aldrich (CC NP), were characterised to understand their surface chemical state using X-ray photoelectron spectroscopy (XPS). Nanopowder was expected to have a core-shell structure, meaning that the metallic core is covered by an oxide shell. The survey spectra for all the nanopowder in as-received form are shown in Figure 13. Survey scans from 0 to 1100 eV binding energy were performed to reveal the various elements present in the near-surface region of the powder. For Fe NP, the survey scan reflected the presence of iron, oxygen and carbon, as indicated by peaks at 711, 530 and 285 eV, respectively. The source of carbon is from the contamination from handling of the nanopowder. The same peaks were observed in the case of steel NP. A peak at 1021 eV, indicating the presence of Zn, was observed for CP NP and may have been a result of manufacturing process. For CC NP, a carbon peak at 284.4 eV was observed along with iron and oxygen; this indicated the presence of graphite on the nanopowder surface when having carbon coating.

The peaks indicating iron in the survey scans could be attributed to iron oxides as well as metallic iron within the core. To differentiate between the states of iron, high resolution XPS was carried out. A metallic iron signal with significant intensity was observed in the high-resolution scan of the surface of Fe NP, CP NP and CC NP at around 707 eV. The presence of the signal from underlying metal suggests that the oxide shell was only a few nanometres thick given that XPS is sensitive to the outer 3 to 5 nm when iron oxide is present. However, the metallic iron signal was absent in steel NP.

The intensity of the signal obtained is proportional to the number of atoms in the analysed region. Hence, the intensities of the oxide and metallic iron peaks in the high-resolution scan could be used to calculate the relative apparent amounts of oxide and metallic iron present, based on which oxide thickness could also be estimated. Different models like planar surface approach with geometric correction for spherical shape [136] [137], A. G. Shard [138] approach were used to fit the data from XPS and determine the oxide thickness. An oxide thickness value of around 3 nm was derived for Fe NP. For steel NP, no such derivation was possible because no metallic iron signal was observed in the as-received surface. To assess the oxide thickness for steel NP, XPS depth profiling was employed, and an oxide thickness of around 15 nm was estimated. The oxide thickness estimation was further complemented by thermogravimetry analysis. The mass loss caused by oxide reduction in pure hydrogen together with the surface area were used to estimate oxide thickness; the values obtained correlated well with the XPS estimation.

Furthermore, high resolution transmission electron microscopy (HRTEM) was performed on Fe NP and CC NP. The core-shell morphology was observed for both Fe NP and CC NP. Iron oxide formed the shell over the metallic iron core and was measured to be 3-4 nm in Fe NP. For CC NP, a graphitic shell encapsulated the iron core. The presence of the core-shell structure and the oxide thickness estimation for Fe NP and CC NP were corroborated by direct observation from the HRTEM micrographs (Figure 14).

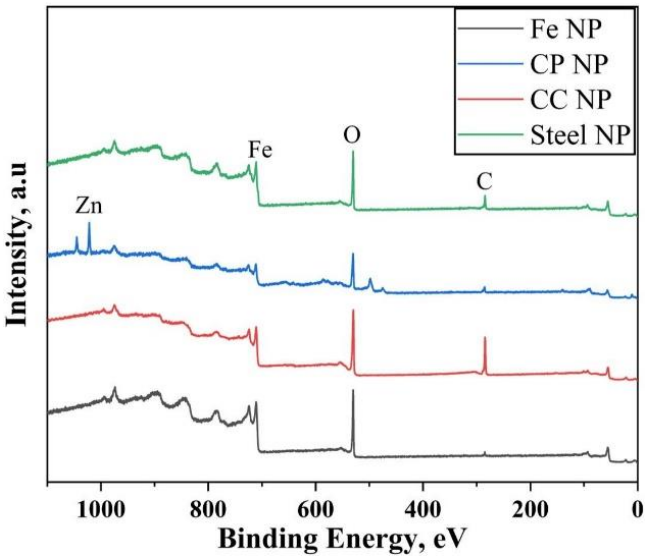

Figure 13: XPS plots showing the survey spectrum for Fe NP, Steel NP, CP NP and CC NP.

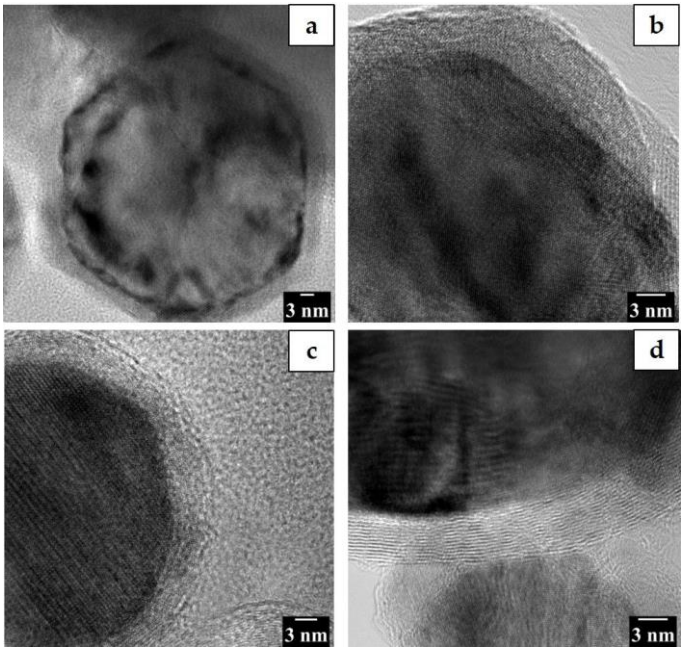

Figure 14: HR TEM micrographs for (a) & (b) Fe NP and (c) & (d) CC NP.

For an efficient sintering process, the surface oxides on metal powder must be reduced for metallurgical bonds to form between the particles, which is crucial for achieving the structural strength of the PM component. An understanding of the oxide reduction characteristics of the nanopowder enables optimised sintering parameters. As such, thermogravimetry experiments were performed on Fe NP in a pure hydrogen atmosphere. Furthermore, iron oxide nanopowder was subjected to similar analysis as a reference material.

During the non-isothermal reduction of the oxide layer of Fe NP, a mass loss of approximately 5% was recorded. The reduction process was initiated at temperatures as low as 300 °C. Complete reduction of the surface oxide was achieved by 600 °C.

These temperatures largely depended on the heating rate, although the slope of the curves remained similar. This mass loss corresponded to the complete reduction of the surface oxide, which was supposed to be mainly Fe_2O_3 reducing to metallic iron. The mass loss, which had a single maximum peak, indicated that the surface oxide was reduced to metallic iron in a single-step process. However, for iron oxide nanopowder, a mass loss of about 30% was observed through a two-step reduction process. The two steps involved are Fe_2O_3 to Fe_3O_4 and Fe_3O_4 to metallic iron.

To understand the reduction kinetics of the oxide scale on the Fe NP, the isoconversional Kissinger-Akahira-Sunose (KAS) method and Kissinger approach were used. To perform these calculations, data was used from mass loss at different heating rates. The apparent activation energy needed for the reduction process was calculated using the two approaches is shown in Figure 15. As seen in Figure 15a-b, the apparent activation energy values from both approaches were in a similar range. With an increase in the Fe NP particle size, a slight increase in activation energy values was observed. The same was true for iron oxide nanopowder (Figure 15c-d). A model was proposed to understand the surface oxide reduction process. In the model, surface iron oxide is reduced to metallic Fe, and the newly formed metallic iron surface accelerates the reduction process by serving as an autocatalytic surface.

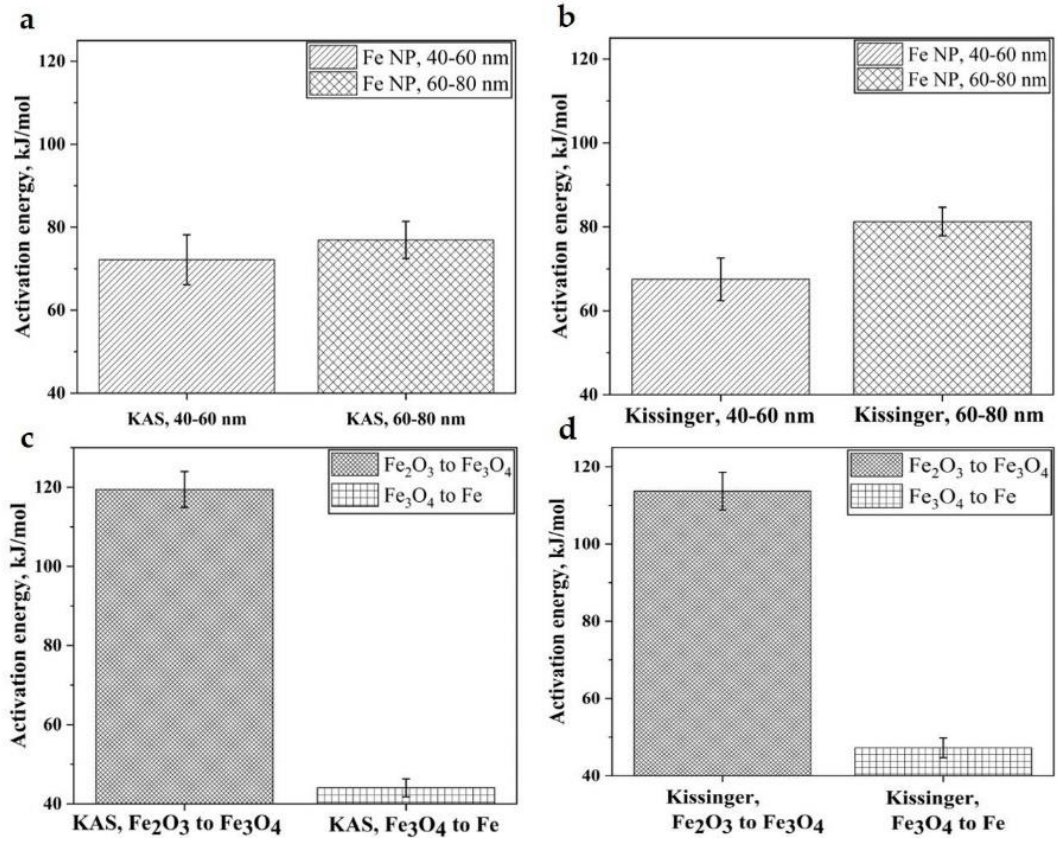

Figure 15: Apparent activation energy values using two different approaches for (a), (b) Fe NP and (c), (d) iron oxide nanopowder.

The reduction behaviour of CC NP (Paper VI) also exhibited distinct behaviour. The reduction rate of CC NP was characterised by multiple peaks that reached higher temperatures than those in Fe NP; this is attributed to the iron oxide's access to hydrogen being blocked by the presence of carbon on the surface, which then participated in the reduction process at higher temperatures.

7.2 Addition of nanopowder to water-atomized iron powder (Papers IV, V and VI)

After investigating the surface characteristics and reduction properties of nanopowder, micrometre-sized powder was added to evaluate the nanopowder influence on sintering. Fe NP, steel NP, CP NP and CC NP were used as the sintering aids. Unless otherwise specified, all the micro/nano bimodal compacts were mixed at a ratio of 95:5 wt.%, with micrometre-sized powder forming the major fraction. Green density was measured before sintering for all the samples (Figure 16). A compaction pressure of 250 MPa was employed for all the variants. The ASC 300+CC NP showed the highest green density, followed by the ASC 300+Fe NP and ASC 300+CP NP compacts. The ASC 300+steel NP had the lowest green density. The steel NP and CP NP were found to be agglomerated. Such agglomeration is considered detrimental and reduces green density. Compared to compacts without nanopowder, the presence of nanopowder decreased powder compressibility. This is supposed to be attributed to the rigidity exerted by the nanopowder, and a consequent reduction in green density was observed. It was also observed that with increasing compaction pressure, the green density of the compacts also increased, as expected.

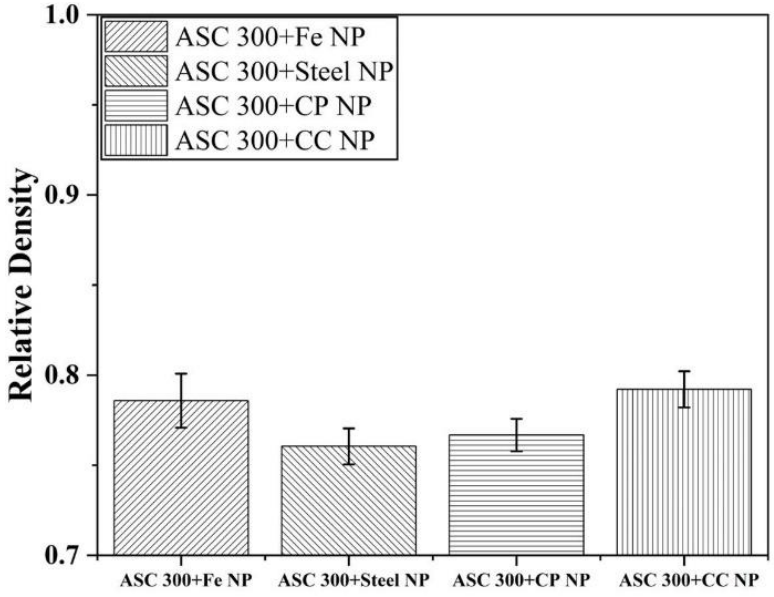

Figure 16: Green density of different micro/nano bimodal powder compacts.

The compacts were subjected to sintering at high temperatures, below the melting point of the base metal, leading to the formation of metallurgical bonds between the metal particles. The compacts were sintered in dilatometer. As such, during sintering, the change in the linear dimension of the compact was measured as a function of time and temperature. The typical shrinkage curve obtained was divided into three stages. During the heating stage of sintering, the material must expand, and the slope of the curve corresponds to the coefficient of thermal expansion. In addition, further sintering can take place during the heating stage, which can be identified by the earlier onset of sintering shrinkage compared to when the target sintering temperature is employed. During the isothermal holding stage, the compact undergoes shrinkage, and during the cooling stage, the compact is expected to thermally shrink. Phase transformation from BCC ferrite (alpha) to FCC austenite (gamma), which is generally observed in iron systems, is also expected in the sinter curves. Figure 17a shows the sintering curve for ASC 300 and ASC 300+Fe NP. The addition of nanopowder increases overall shrinkage. Though the outlines of the sinter curves were similar, a clear deviation in their nature was apparent, represented by the highlighted region in Figure 17a. Higher magnification, as shown in Figure 17b, depicts the difference in shape due to the presence of Fe NP as no other parameters were changed. This suggests that the thermal expansion expected during the heating phase is compensated by sintering. It should be noted that the deviation between the two compacts initiates at temperatures as low as 600 °C. Thus, sintering at intermittent temperatures starting from 500 °C was undertaken. The sintered compacts were then subjected to fractography to understand the underlying reason for the deviation in sintering behaviour. As seen in Figure 17c, the nanopowder was discernible and devoid of any necking between particles. When heated to 700 °C, nanopowder coalescence was observed (Figure 17d). Additionally, the nanopowder was sintered onto neighbouring coarse particles.

To further study the sintering behaviour of micro/nano bimodal powder compacts, a master sintering curve model was used, which is used to predict the sintering behaviour. Differences were observed between the experimental data and model that are attributed to the phase transformation involved in the iron system as well as the multiple peak shrinkage behaviour with the addition of nanopowder. It was concluded that the approach could not be used to produce master sintering curves for ASC 300 and ASC+Fe NP sintered compacts.

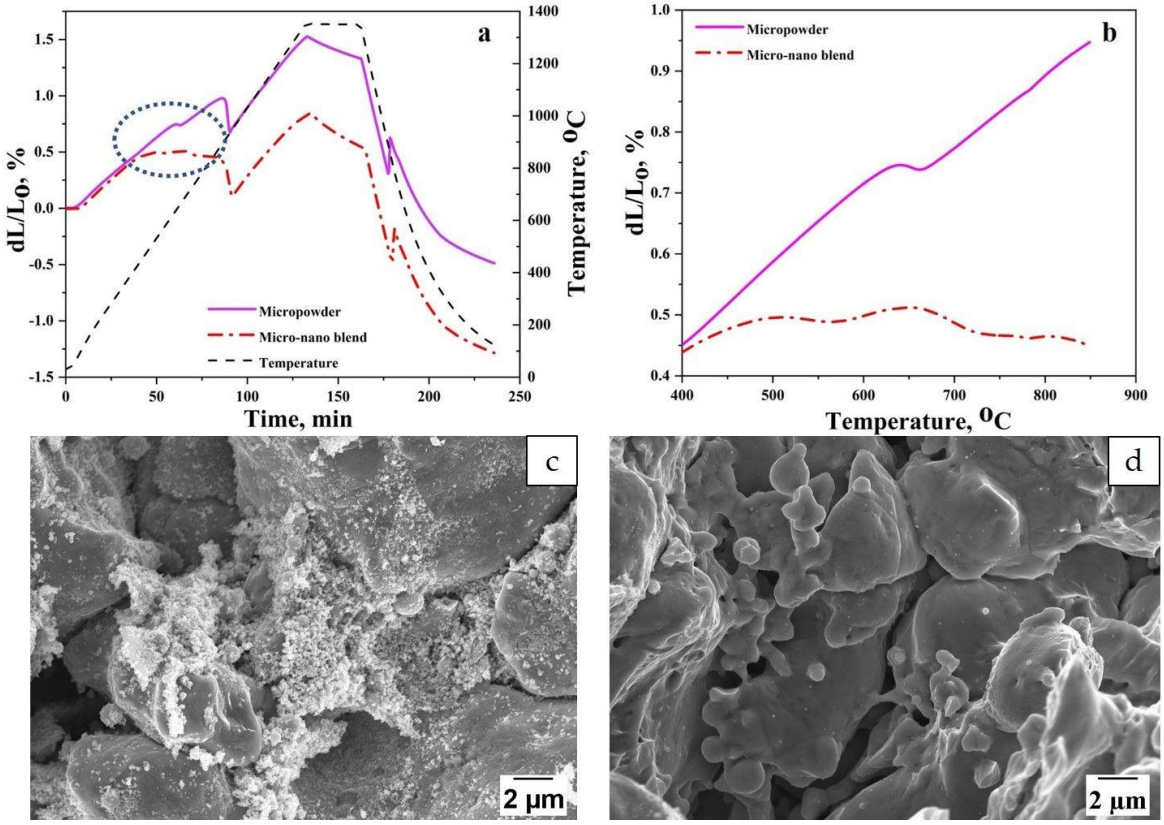

Figure 17: (a) Sinter curves of both micro and micro/nano bimodal powder compact sintered with final target temperature of 1350 °C; (b) higher magnification of 17a showing the difference in sintering behaviour due to the presence of nanopowder in the compact (see Paper IV), (c) and (d) scanning electron micrographs showing the evolution of the microstructure of the ASC 300+Fe NP compact sintered at 500 °C and 700 °C, respectively.

The addition of carbon as well as nanopowder was also explored. For the first approach, Steel NP with added carbon, CP NP and CC NP were employed. For CC NP, apart from carbon serving as an alloying element and reducing agent, the possibility of modifying and the temperature at which nanopowder sintering was explored. For CC NP, the probable decrease in agglomeration tendency of the nanopowder due to the presence of carbon on the surface can also be explored in the future. In the second approach, the carbon sources of natural graphite (PG10) and synthetic graphite (KS4) were added to an ASC 300+Fe NP mixture to understand the combined impact on the sintering. Figure 18a shows the sinter curves of both ASC 300+CP NP and ASC 300+CC NP compacts sintered with final temperature of 1250 °C. The linear shrinkage obtained from the compact containing CP NP was lower in comparison to the compact containing CC NP. This could be attributed to the detrimental effect caused by the agglomeration of nanopowder when having CP NP. Similar results were seen for ASC 300+steel NP sintered compacts. The lower linear shrinkage values could be attributed to the physical and chemical characteristics of the nanopowder chosen, such as higher agglomeration tendency and prevalent oxides

in surface chemistry. Figure 18b shows the sinter curves of the compacts obtained through carbon addition. Linear shrinkage was the same in both approaches.

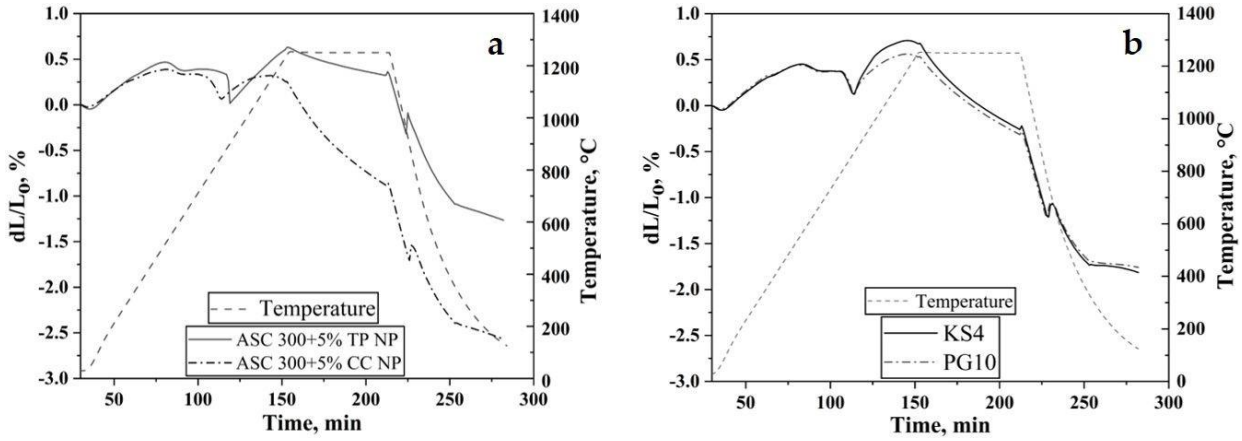

Figure 18: Sinter curves of compacts sintered at 1250 °C in pure hydrogen environment for (a) ASC 300+CP NP and ASC 300+CC NP and (b) ASC 300+Fe NP+PG 10 and ASC 300+Fe NP+KS4.

7.3 Addition of nanopowder to chromium pre-alloyed water-atomized steel powder (Papers VII, VIII and IX)

The addition of nanopowder to micrometre-sized powder was extended to chromium pre-alloyed water-atomized steel powder, which is used in high-performance applications. Chromium pre-alloyed steel powder with 1.8 wt.% chromium, admixed with 2 wt.% nickel and 0.3 wt.% carbon served as the base powder. Fully pre-alloyed powder has high hardness and reduced compressibility. Therefore, apart from pre-alloying with chromium, alloying elements are added and mixed in the form of elemental powder to maintain a high level of compressibility. In the present case, a fine powder form of nickel was admixed to the chromium pre-alloyed powder. Fe NP was also mixed with this base powder, and the resulting powder mix was subjected to compaction and sintering. After this, the impact of various parameters, including the impact of the addition of nanopowder on densification, was evaluated using a design of experiments approach. The results indicated that the increase in sintering temperature followed by nanopowder addition improved the sintered density.

Based on microstructural analysis, following compaction at similar pressures, the misorientation at particle boundaries in the compacts containing nanopowder was higher compared to those where nanopowder was absent. It can be inferred that this phenomenon also contributed to the higher shrinkage and densification achieved.

Compacts pressed under two different conditions were sintered and analysed; laboratory scale compaction and industrial scale compaction - with the former yielding lower green densities than the latter. Sintering results from laboratory-

pressed compacts are presented in Figure 19a. The curves followed the same trend seen for the iron/iron micro/nano bimodal powder compacts studied in Papers IV, V and VI; that is, the compact containing nanopowder had a higher linear shrinkage than the compact without nanopowder. Figure 19b-c shows the microstructures of CrA+Ni+C and CrA+Ni+C+Fe NP compacts sintered at 1250 °C. The microstructures were constituted by ferrite, bainite, martensite and pearlite. The fraction of ferrite was higher in compacts containing Fe NP. Chemical analysis showed that the carbon content of the CrA+Ni+C+Fe NP compact after sintering was less than that of the CrA+Ni+C compact. This was expected because nanopowder contributes to higher initial oxygen content, the more extensive oxide reduction of which causes higher carbon loss. This study also provides guidelines for appropriate alloying. The addition of Fe NP slightly decreased the overall alloying content of the micro/nano bimodal powder compared to only CrA+Ni+C powder mix alone. A detailed study on the microstructural evolution of the two sintered compacts was performed and reported in Paper VIII. The microstructural observations were complemented with JMatPro simulations in order to understand the impact of nanopowder on the content and distribution of microstructural constituents. Moreover, the evaluation of the impact of Fe NP on the distribution of Ni was discussed utilising the idea of "effective" nickel addition in the compacts.

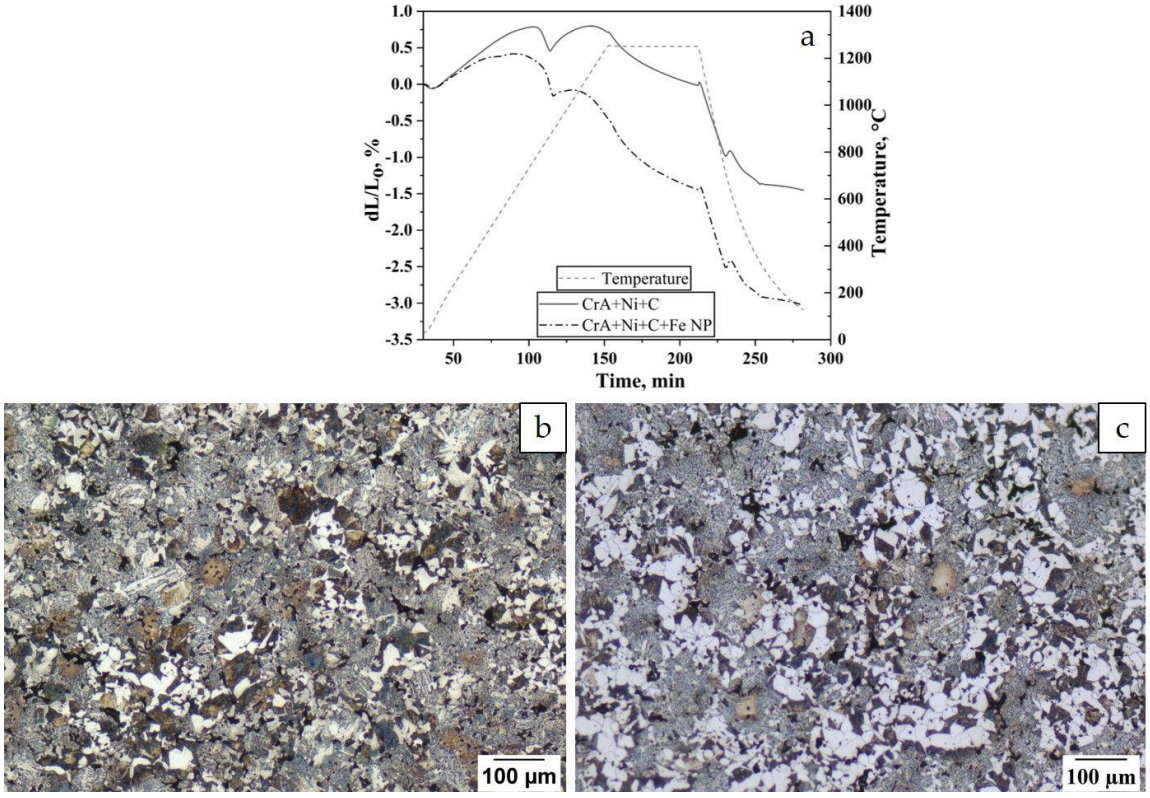

Figure 19: (a) Sintering curves of CrA+Ni+C and CrA+Ni+C+Fe NP compacts sintered at 1250 °C, (b) and (c) microstructure of CrA+Ni+C and CrA+Ni+C+Fe NP sintered compacts showing different constituents.

A similar study was performed with the compaction performed under industrial conditions in which the compacts with and without nanopowder were pressed to the same green density. After subsequent sintering, a marginal increase in linear shrinkage was observed, but this was lower than the shrinkage in laboratory scale compaction in terms of both linear shrinkage and sintered density with the presence of nanopowder. The decrease in the effectiveness of nanopowder addition compared to earlier studies in the laboratory scale is attributed to potential nanoparticle coarsening/sintering and delayed reduction of surface oxide.

CHAPTER 8

CONCLUSIONS

What are the surface characteristics of nanopowder, and how can the surface oxide thickness be determined?

- Different models were used to evaluate the XPS data, and a methodology was established to measure the thickness of surface oxide on nanopowder.
- All the models except the depth profiling technique yielded an oxide thickness of approximately 3 nm for Fe iron nanopowder. Through HR TEM, it was observed that the iron core was covered by an oxide shell whose thickness was 3-4 nm. This was well in agreement with the XPS and thermogravimetric results.
- For the case of steel nanopowder, thicker oxide scale well above 3 nm was expected.
- Carbon-coated nanopowder revealed iron core entirely coated by multilayer carbon shell. The inter-planar spacing is measured to be around 0.30-0.35 nm, which is similar to the value of graphite. The carbon peak at 284.4 eV from XPS results supports the presence of graphitic layers further.

Which mechanisms are involved in the surface oxide reduction of iron nanopowder, and how can they be evaluated?

- For all the heating rates, from 5 to 50 °C/min, mass losses of approximately 5% and 30% were recorded for the iron and iron oxide nanopowder, respectively.
- For iron nanopowder, a single reduction step from Fe_2O_3 to Fe was observed, whereas in the case of iron oxide nanopowder, the reduction process followed a two-stage process.
- The activation energy for the first stage was in the range of 105 to 120 kJ/mol, after which the values decrease to as low as 45 kJ/mol during the final reduction step. The activation energy values recorded for the reduction of surface oxide for iron nanopowder were from 60 to 120 kJ/mol.
- The reduced activation energy was attributed to the catalytic activity of reduced Fe particles, which facilitate the reduction of the adjacent oxide remains.

How does the addition of nanopowder influence the compaction and sintering behaviour of water-atomized iron powder?

- The presence and increase in nanopowder content decreased the compressibility of the micro/nano bimodal powder in proportional to the nanopowder content.

- The sinter curve correlated with the presence of nanopowder, implying that nanopowder influenced sintering behaviour.
- The compact containing nanopowder showed shrinkage at temperatures as low as 500 °C.
- The fractographic analysis of the compacts that underwent sintering at intermittent temperatures also revealed that nanopowder in the compact sintered at temperatures between 500 °C and 700 °C.
- Increased nanopowder content resulted in increased densification in the sinter compacts. The allotropic transformation involved with iron as well as the multi-peak shrinkage behaviour of nanopowder makes it difficult to use the conventional master sintering curve model to describe sintering behaviour.
- Improved linear shrinkage was observed in the sintered compact containing carbon-coated iron powder versus iron nanopowder containing sintered compact. The carbon coating on the iron nanopowder may have inhibited the sintering enhancement by nanopowder by reducing the diffusivity.

How does the addition of nanopowder affect the sintering of steel powder intended for commercial applications?

- The linear shrinkage during sintering increased for chromium pre-alloyed steel powder compacts with the addition of nanopowder. The increase in sintering temperature and the addition of nickel also improved densification.
- An increase in ferrite content was observed in the sintered compact containing iron nanopowder. This is due to decrease in carbon content in sintered compact with iron nanopowder and is explained through the reduction of excess oxygen present in the form of surface oxides of iron nanopowder.
- The effective nickel content was higher in the compact containing iron nanopowder showing that the nanopowder provides the grain boundary network for better distribution of nickel.
- Higher compaction pressure was needed to compact the nanopowder containing powder in comparison to the powder without nanopowder in order to reach the same green density. Sintered density values revealed that the compact containing iron nanopowder showed marginally higher density in comparison to the compact without nanopowder. No major difference was observed in impact energy values between these two variants.

CHAPTER 9

FUTURE SCOPE

This work explored the concept of using nanopowder as a sintering aid for press and sinter powder metallurgy (PM) steel. This study focused primarily on how nanopowder influences the sintering and the characteristics of nanopowder. The results indicate that the sintered density achieved through this work was marginally short of the desired 95% relative density needed to use hot isostatic pressing (HIP) without a capsule. Nevertheless, with improved densification of the base powder, the proven effects of nanopowder could constitute an important means of securing a final percentage increase of sintering to reach 95% relative density. It would also be desirable to investigate different compositions of nanopowder and to compare the liquid phase sintering approach where a master alloy is employed. Towards the end of this research work, some promising results were seen when the using carbon-coated nanopowder versus pure iron nanopowder. Further investigation with varying proportions of carbon would be interesting. On the compaction front, cold isostatic compaction (CIP) needs further exploration as limited trials were undertaken in this study, where the benefit of CIP in avoiding lubricant is an important means of further improving green density prior to sintering.

As for demonstrating the technology of using nanopowder as a sintering aid, physical demonstration is to be manufactured. The combination of CIP, sintering and HIP is the proposed manufacturing route for parts that would then be subjected to a surface-hardening treatment. This processing route allows the possibility of reaching full density fabrication, and the results of the present thesis have laid a platform how nanopowder could constitute a part of a future solution.

Beyond densification, hardenability is another important factor to consider for improving the adaptability of press and sinter PM steel in newer applications. While pre-alloyed powder provides both good hardenability and microstructure uniformity, significant hardness levels in the powder are incurred leading to technological challenges for their compaction. One possibility is to evaluate the addition of nanopowder in pre-alloyed powder with higher alloying content than is generally industrially accepted but pressed to a lower density to compensate for densification through the sintering aid.

Typically, shrinkage during sintering is undesirable in components produced through press and sinter steel because strict dimensional tolerances should be maintained, and

a near-final shape is obtained after compaction. One major challenge when nanopowder is added as a sintering aid is that shrinkage effects during sintering lead to dimensional changes in the components. Compensating for these dimensional changes and shrinkage through the addition of appropriate alloying should be explored.

ACKNOWLEDGEMENTS

First and foremost, I would like to thank my supervisor and examiner Professor Lars Nyborg for his efforts, investment, guidance and constant encouragement. I would also like to thank my co-supervisor Professor Eduard Hryha for providing timely feedback and discussions. Thank you for providing me with an opportunity to carry out research in the Department of Industrial and Materials Science. I would like to acknowledge the Swedish Foundation for Strategic Research (SSF) for granting funding within the framework of the grant GMT 14-0045 "Nanotechnology Enhanced Sintered Steel Processing".

I would like to thank Dr Dimitris Chasoglou and Lic Eng Dmitri Riabov at Höganäs AB for their support powder supply and compaction. I would also like to recognise Professor Johan Liu and Lic Eng Abdelhafid Zehri for their assistance with regard to nano additives within the framework of the mentioned SSF project.

Furthermore, I would like to thank Dr Johan Wendel and Dr Maheswaran Vattur Sundaram for all their help, collaboration and conversations about powder. Special regards to Mr. Bala Malladi for the collaboration and support with microscopy. I would like to express my utmost gratitude to Professor Fang Liu for all her support with HRTEM characterisation.

Thank you to Dr Ruslan Shvab and Professor Yu Cao for their guidance regarding surface characterization and to Dr Eric Tam, Dr Yiming Yao and Mr Roger Saghdahl for all their help and support.

I would like to take this opportunity to thank Dr T. K. Nandy, Mr Abhay K. Jha and Dr Ramesh Narayanan for introducing me to the world of materials research. Thank you for guiding me in this direction! Special thanks to NPTEL.

My appreciation to my colleagues in the department of industrial and materials science for creating a pleasant environment. I would like to thank Dr Antonio Mulone for the help with EBSD. Special thanks to my past and present officemates Giulio, Mahesh and Bala for keeping the office space lively. Special thanks also go to Elango, Sukhdeep, Adrianna and Dinesh. I would like to thank Sarmista and Vishnu.

I'm extremely grateful to Ajay for all the support he gave me after moving to Sweden and for the 'supervising' sessions which in hindsight worked. For all the travels, food, games, walks and movies!

I thank my friends and cousins Gayathri, Soumya, MS, Kiran, Ravi, Akka, CM, KS, Swathy, CK, Sampath, Raja and AS back home in India and in other parts of the world for always having my back and for all the fun and happy times together. These times have kept me going!

I'm thankful to the GR network for all the interesting discussions which helped me to grow as an individual. I'm hopeful that this collaboration will help me further with reading.

I’m grateful to my extended family for their constant encouragement during all my endeavours up to this point, including my aunts who have been waiting for me to take this degree. Special thanks to my Parents, Karthik and Seshendra, for their patience, support and understanding throughout my journey.

To all the people who put their trust in me!

To all the women who inspired me!

To Amma and Nanna!

To All who believed in me!

Swathi Kiranmayee Manchili

2021-08-03

ఎందరో మహానుభావులు అందరికీ వందనములు - త్యాగరాజ స్వామి

endarō mahānubhāvulu andariki vandanamulu- tyāgarāja swāmi

REFERENCES

[1] Höganäs Handbook for Sintered Components-3. Design and Properties, Höganäs AB, 2004.

[2] M. Vattur Sundaram, Novel approaches for acheiving full density powder metallurgy steels, Chalmers University of Technology, 2019.

[3] R.D.O. Calderón, E. Bernardo, M. Campos, C. Gierl-Mayer, H. Danninger, J.M. Torralba, Tailoring master alloys for liquid phase sintering: Effect of introducing oxidation-sensitive elements, Powder Metall. 59 (2016) 31–40. https://doi.org/10.1080/00325899.2016.1148897.

[4] R.M. German, P. Suri, S.J. Park, Review: Liquid phase sintering, J. Mater. Sci. 44 (2009) 1–39. https://doi.org/10.1007/s10853-008-3008-0.

[5] J.-P. Choi, H.-G. Lyu, W.-S. Lee, J.-S. Lee, Densification and microstructural development during sintering of powder injection molded Fe micro–nanopowder, Powder Technol. 253 (2014) 596–601. https://doi.org/https://doi.org/10.1016/j.powtec.2013.11.048.

[6] A. Zehri, Manufacturing and characterization of nanomaterials for low-temperature sintering and electronics thermal management applications, 2020.

[7] J. Wendel, Sintering of water-atomized iron and low-alloyed steel powder, Chalmers University of Technology, 2020.

[8] E. Bergstedt, A Comparative Investigation of Gear Performance Between Wrought and Sintered Powder Metallurgical Steel, KTH Royal Institute of Technology, 2021.

[9] A. Holmberg, M. Andersson, Å.K. Rudolphi, Rolling fatigue life of PM steel with different porosity and surface finish, Wear. 426–427 (2019) 454–461. https://doi.org/https://doi.org/10.1016/j.wear.2019.01.006.

[10] B. Kianian, A comparative cost analysis of conventional wrought steel and powder metallurgy (PM) gear manufacturing technologies, 2019.

[11] W.D. Kingery, Sintering from Prehistoric Times to the Present, in: Sinter. '91, Trans Tech Publications, 1992: pp. 1–10. https://doi.org/10.4028/www.scientific.net/SSP.25-26.1.

[12] P. Ramakrishnan, History of Powder Metallurgy, Indian J. Hist. Sci. 18 (1983) 109–114. https://doi.org/https://doi.org/10.1016/B978-1-85617-422-0.50010-X.

[13] Economic Considerations for Powder Metallurgy Structural Parts, (n.d.). https://www.pm-review.com/introduction-to-powder-metallurgy/economic-considerations-for-powder-metallurgy-structural-parts/ (accessed October 29, 2018).

[14] F.G. Hanejko, Warm compaction, in: ASM Handb. Powder Met. Technol. Appl., 1998: pp. 376–381. https://doi.org/10.1016/S0026-0657(01)80051-5.

[15] European Powder Metallurgy Association (EPMA) - Powder Manufacture, (n.d.). https://www.epma.com/powder-metallurgy-powder-manufacture (accessed October 29, 2018).

[16] K. Skotnicová, M. Kursa, I. Szurman, Powder Metallurgy, 2014. https://doi.org/10.1038/190572a0.

[17] E. Peter, W. Lee, ASM Handbook: Volume 7: Powder Metal Technologies and Applications, in: P. Ed, L. W (Eds.), 1st ed., ASM International, 1998: p. 1147.

[18] Powder production - LPW Technology, (n.d.). https://www.lpwtechnology.com/technical-library/powder-production/ (accessed October 30, 2018).

[19] The Water-Atomizing Process: Part One, (n.d.). https://www.totalmateria.com/page.aspx?ID=CheckArticle&site=ktn&NM=309 (accessed May 1, 2021).

[20] Höganäs, Material and powder properties, in: Höganäs Handbook. Sintered Components, 2013: p. 86.

[21] J. Wendel, Characteristics and Sintering of Fine Water-atomized and Carbonyl Iron Powder, Chalmers University of Technology, 2018.

[22] S. Karamchedu, Delubrication of Chromium Prealloyed Powder Metallurgy Steels, Chalmers University of Technology, 2013.

[23] Design Considerations with Powder Metallurgy | PickPM, (n.d.). https://www.pickpm.com/design-resource-center/design-considerations/ (accessed October 30, 2018).

[24] Power Metallurgy - Advantages and Limitations, (n.d.). https://www.eit.edu.au/cms/resources/technical-resourses/power-metallurgy-advantages-and-limitations (accessed October 27, 2018).

[25] Powder Metallurgy Advantages: Why Use Powder Metallurgy? | PickPM, (n.d.). https://www.pickpm.com/introduction-powder-metallurgy/advantages-powder-metallurgy/ (accessed October 27, 2018).

[26] A. Panda, J. Dobransky, M. Jancik, I. Pandova, M. Kacalova, Advantages and Effectiveness Of The Powder, Metalurgija. 57 (2018) 353–356.

[27] Why Powder Metallurgy?, (n.d.). https://www.pm-review.com/introduction-to-powder-metallurgy/why-powder-metallurgy/ (accessed October 27, 2018).

[28] Powder Metallurgy | Process, Advantages, Disadvantages, Applications, (n.d.). https://clubtechnical.com/powder-metallurgy (accessed October 26, 2018).

[29] Powder Metallurgy Process with its Advantages and Disadvantages - mech4study, (n.d.). http://www.mech4study.com/2017/05/powder-metallurgy-process.html (accessed October 31, 2018).

[30] W.A. Kaysser, W. Weise, Powder Metallurgy and Sintered Materials, Ullmann's Encycl. Ind. Chem. (2000). https://doi.org/10.1002/14356007.a22_105.

[31] J.M. Cullen, J.M. Allwood, M.D. Bambach, Mapping the Global Flow of Steel: From Steelmaking to End-Use Goods, Environ. Sci. Technol. 46 (2012) 13048–13055. https://doi.org/10.1021/es302433p.

[32] J.M.C. Azevedo, A. CabreraSerrenho, J.M. Allwood, Energy and material efficiency of steel powder metallurgy, Powder Technol. 328 (2018) 329–336. https://doi.org/https://doi.org/10.1016/j.powtec.2018.01.009.

[33] H. Danninger, What will be the future of powder metallurgy?, Powder Metall. Prog. 18 (2018) 70–79. https://doi.org/10.1515/pmp-2018-0008.

[34] F. Persson, A. Eliasson, P.G. Jönsson, Oxidation of Water Atomized Metal Powders, Steel Res. Int. 85 (n.d.) 1629–1638. https://doi.org/10.1002/srin.201300466.

[35] L. Nyborg, T. Tunberg, P.X. Wang, Surface product formation during water atomization and sintering of austenitic stainless steel powder, Met. Powder Rep. 45 (1990) 750–753. https://doi.org/https://doi.org/10.1016/0026-0657(90)90459-T.

[36] V. Kruzhanov, V. Arnhold, Energy consumption in powder metallurgical manufacturing, Powder Metall. 55 (2012) 14–21. https://doi.org/10.1179/174329012X13318077875722.

[37] E. Hryha, E. Dudrova, S. Bengtsson, Influence of powder properties on compressibility of prealloyed atomised powders, Powder Metall. 51 (2008) 340–342. https://doi.org/10.1179/174329008X286596.

[38] M. Hull, Astaloy CrM: new generation powder from Höganäs, Powder Metall. 41 (1998) 227–238. https://doi.org/10.1179/pom.1998.41.4.227.

[39] E. Hryha, L. Cajkova, E. Dudrova, L. Nyborg, Study of reduction/oxidation processes in Cr-Mo prealloyed steels during sintering by continuous atmosphere monitoring, Proc. Euro Int. Powder Metall. Congr. Exhib. Euro PM 2008. 1 (2008) 109–114.

[40] W.B. James, Ferrous Powders - How Alloying Method Influences Sintering, in: MPIF Sinter. Semin., Pttsburgh, USA, 1991: pp. 1–23.

[41] V.A. Krokha, A.M. Bakhovkin, An advanced method for the manufacture of gears (review), Sov. Powder Metall. Met. Ceram. 2 (1964) 81–85. https://doi.org/10.1007/BF00774142.

[42] M. Vattur Sundaram, A. Khodaee, M. Andersson, L. Nyborg, A. Melander, Experimental and finite element simulation study of capsule-free hot isostatic pressing of sintered gears, Int. J. Adv. Manuf. Technol. 99 (2018) 1725–1733. https://doi.org/10.1007/s00170-018-2623-4.

[43] A. Hadrboletz, B. Weiss, Fatigue behaviour of iron based sintered material: a review, Int. Mater. Rev. 42 (1997) 1–44. https://doi.org/10.1179/imr.1997.42.1.1.

[44] L. Zhang, Z. Liu, H. Sun, M. Qin, X. Qu, Y. Lyu, Dynamic properties of high-density low-alloy PM steels, Powder Metall. 60 (2017) 56–65. https://doi.org/10.1080/00325899.2016.1274815.

[45] M. Andersson, M. Larsson, Linking pore size and structure to the fatigue performance of sintered steels, Proc. World Powder Metall. Congr. Exhib. World PM 2010. 3 (2010) 1–8.

[46] G. Cipolloni, C. Menapace, I. Cristofolini, A. Molinari, A quantitative characterisation of porosity in a Cr–Mo sintered steel using image analysis, Mater. Charact. 94 (2014) 58–68. https://doi.org/https://doi.org/10.1016/j.matchar.2014.05.005.

[47] S. Dizdar, High-Performance Sintered-Steel Gears for Transmissions and Machinery : A Critical Review, Gear Technol. (2012) 60–65.

[48] A. Flodin, M. Andersson, A. Miedzinski, Full density powder metal components through Hot Isostatic Pressing, Met. Powder Rep. 72 (2017) 107–110. https://doi.org/https://doi.org/10.1016/j.mprp.2016.02.057.

[49] K. Essa, P. Jamshidi, J. Zou, M.M. Attallah, H. Hassanin, Porosity control in 316L stainless steel using cold and hot isostatic pressing, Mater. Des. 138 (2018) 21–29. https://doi.org/https://doi.org/10.1016/j.matdes.2017.10.025.

[50] H. Hassanin, A.A. Al-Kinani, A. ElShaer, E. Polycarpou, M.A. El-Sayed, K. Essa, Stainless steel with tailored porosity using canister-free hot isostatic pressing for improved osseointegration implants, J. Mater. Chem. B. 5 (2017) 9384–9394. https://doi.org/10.1039/C7TB02444D.

[51] A. Eklund, M. Ahlfors, Heat treatment of PM parts by Hot Isostatic Pressing, Met. Powder Rep. 73 (2018) 163–169. https://doi.org/https://doi.org/10.1016/j.mprp.2018.01.001.

[52] M. Dlapka, H. Danninger, C. Gierl, B. Lindqvist, Defining the pores in PM components, Met. Powder Rep. 65 (2010) 30–33. https://doi.org/10.1016/S0026-0657(10)70093-X.

[53] H. Karlsson, L. Nyborg, S. Berg, Surface chemical analysis of prealloyed water atomised steel powder, Powder Metall. 48 (2005) 51–58. https://doi.org/10.1179/0032589005X37675.

[54] D. Chasoglou, Surface Chemical Characteristics of Chromium-alloyed Steel Powder and the Role of Process Parameters during Sintering, Chalmers University of Technology, 2012. http://publications.lib.chalmers.se/publication/157463?pubid=128185.

[55] E. Hryha, C. Gierl, L. Nyborg, H. Danninger, E. Dudrova, Surface composition of the steel powders pre-alloyed with manganese, Appl. Surf. Sci. 256 (2010) 3946–3961. https://doi.org/https://doi.org/10.1016/j.apsusc.2010.01.055.

[56] J. Wendel, R. Shvab, Y. Cao, E. Hryha, L. Nyborg, Surface analysis of fine water-atomized iron powder and sintered material, Surf. Interface Anal. 50 (2018) 1065–1071. https://doi.org/https://doi.org/10.1002/sia.6455.

[57] P. Rodgers, Nanoelectronics: Single file, Nat. Nanotechnol. (2006). https://doi.org/10.1038/nnano.2006.5.

[58] H. Rauscher, G. Roebben, H. Rauscher, G. Roebben, A.B. Sanfeliu, H. Emons, N. Gibson, R. Koeber, T. Linsinger, K. Rasmussen, J.R. Sintes, B. Sokull-klüttgen, H. Stamm, Towards a review of the EC Recommendation for a definition of the term "nanomaterial" - Part 3 - Scientific-technical evaluation of options to clarify the definition and to facilitate its implementation, 2015. https://doi.org/10.2788/678452.

[59] L.A. Kolahalam, I. V Kasi Viswanath, B.S. Diwakar, B. Govindh, V. Reddy, Y.L.N. Murthy, Review on nanomaterials: Synthesis and applications, Mater. Today Proc. 18 (2019) 2182–2190. https://doi.org/https://doi.org/10.1016/j.matpr.2019.07.371.

[60] Maiti, Bidinger, A new integrated approach for risk assessment and management of nanotechnologies, 2017.

[61] Future challenges related to the safety of manufactured nanomaterials, 2016.

[62] L. Jackson, Radiation safety aspects of nanotechnology, 2017.

[63] C. Suryanarayana, C.C. Koch, Chapter 12 Nanostructured materials, Pergamon Mater. Ser. 2 (1999) 313–344. https://doi.org/10.1016/S1470-1804(99)80058-3.

[64] R. Birringer, U. Herr, H. Gleiter, Nanocrystalline Materials - A First Report, in: Trans. Japan Inst. Met. Suppl., 1986: pp. 43–52.

[65] X. Zhu, R. Birringer, U. Herr, H. Gleiter, X-ray diffraction studies of the structure of nanometer-sized crystalline materials, Phys. Rev. B. 35 (1987) 9085–9090. https://doi.org/10.1103/PhysRevB.35.9085.

[66] S. Suwas, A. Bhowmik, S. Biswas, Ultra-fine Grain Materials by Severe Plastic Deformation: Application to Steels BT - Microstructure and Texture in Steels, in: A. Haldar, S. Suwas, D. Bhattacharjee (Eds.), Springer London, London, 2009: pp. 325–344.

[67] S. Iwama, K. Hayakawa, T. Arizumi, Growth of ultrafine particles of transition metal nitrides by the reactive gas evaporation technique with electron beam heating, J. Cryst. Growth. 66 (1984) 189–194. https://doi.org/https://doi.org/10.1016/0022-0248(84)90090-3.

[68] C. Suryanarayana, G.E. Korth, Consolidation of nanocrystalline powders, Met. Mater. 5 (1999) 121–128. https://doi.org/10.1007/BF03026041.

[69] F. Kim, S. Connor, H. Song, T. Kuykendall, P. Yang, Platonic Gold Nanocrystals, Angew. Chemie Int. Ed. 43 (2004) 3673–3677. https://doi.org/https://doi.org/10.1002/anie.200454216.

[70] S. Mourdikoudis, R.M. Pallares, N.T.K. Thanh, Characterization techniques for nanoparticles: Comparison and complementarity upon studying nanoparticle properties, Nanoscale. 10 (2018) 12871–12934. https://doi.org/10.1039/c8nr02278j.

[71] J. Horváth, Diffusion in Nanocrystalline Materials, in: Diffus. Met. Alloy. (DIMETA 88), Trans Tech Publications Ltd, 1991: pp. 207–228. https://doi.org/10.4028/www.scientific.net/DDF.66-69.207.

[72] Z.Z. Fang, H. Wang, Densification and grain growth during sintering of nanosized particles, Int. Mater. Rev. 53 (2008) 326–352. https://doi.org/10.1179/174328008X353538.

[73] J. Sun, S.L. Simon, The melting behavior of aluminum nanoparticles, Acta Mater. 463 (2007) 32–40. https://doi.org/10.1016/j.tca.2007.07.007.

[74] J.M. Balbus, A.D. Maynard, V.L. Colvin, V. Castranova, G.P. Daston, R.A. Denison, K.L. Dreher, P.L. Goering, A.M. Goldberg, K.M. Kulinowski, N.A. Monteiro-Riviere, G. Oberdörster, G.S. Omenn, K.E. Pinkerton, K.S. Ramos, K.M. Rest, J.B. Sass, E.K. Silbergeld, B.A. Wong, Meeting Report: Hazard Assessment for Nanoparticles 2014; Report from an Interdisciplinary Workshop, Environ. Health Perspect. 115 (2007) 1654–1659. https://doi.org/10.1289/ehp.10327.

[75] W.G. Kreyling, M. Semmler, W. Möller, Dosimetry and Toxicology of Ultrafine Particles, J. Aerosol Med. 17 (2004) 140–152. https://doi.org/10.1089/0894268041457147.

[76] R.D. Brook, B. Franklin, W. Cascio, Y. Hong, G. Howard, M. Lipsett, R. Luepker, M. Mittleman, J. Samet, S.C. Smith, I. Tager, Air Pollution and Cardiovascular Disease, Circulation. 109 (2004) 2655–2671. https://doi.org/10.1161/01.CIR.0000128587.30041.C8.

[77] J.W. Oh, Y. Seong, D.S. Shin, S.J. Park, Investigation and two-stage modeling of sintering behavior of nano/micro-bimodal powders, Powder Technol. 352 (2019) 42–52. https://doi.org/https://doi.org/10.1016/j.powtec.2019.04.056.

[78] J. Rajabi, N. Muhamad, A.B. Sulong, Effect of nano-sized powders on powder injection molding: a review, Microsyst. Technol. 18 (2012) 1941–1961. https://doi.org/10.1007/s00542-012-1631-9.

[79] G.-D. Sun, K.-F. Wang, C.-M. Song, G.-H. Zhang, A low-cost, efficient, and industrially feasible pathway for large scale preparation of tungsten nanopowders, Int. J. Refract. Met. Hard Mater. 78 (2019) 100–106. https://doi.org/10.1016/j.ijrmhm.2018.08.013.

[80] F. Tavangarian, A. Fahami, G. Li, M. Kazemi, A. Forghani, Structural characterization and strengthening mechanism of forsterite nanostructured scaffolds synthesized by multistep sintering method, J. Mater. Sci. Technol. 34 (2018) 2263–2270. https://doi.org/10.1016/j.jmst.2018.06.010.

[81] J.M. Park, J.S. Han, C.W. Gal, J.W. Oh, J.H. Kim, K.H. Kate, S. V Atre, Y. Kim, S.J. Park, Fabrication of micro-sized piezoelectric structure using powder injection molding with separated mold system, Ceram. Int. 44 (2018) 12709–12716. https://doi.org/10.1016/j.ceramint.2018.04.073.

[82] J.S. Han, C.W. Gal, J.H. Kim, S.J. Park, Fabrication of high-aspect-ratio micro piezoelectric array by powder injection molding, Ceram. Int. 42 (2016) 9475–9481. https://doi.org/10.1016/j.ceramint.2016.03.011.

[83] C. Wang, Z. Lu, K. Zhang, Fabrication of Micro-Parts with High-Aspect Ratio Micro-Hole Array by Micro-Powder Injection Molding, Materials (Basel). 11 (2018). https://doi.org/10.3390/ma11101864.

[84] C. Shearwood, Y.Q. Fu, L. Yu, K.A. Khor, Spark plasma sintering of TiNi nanopowder, Scr. Mater. 52 (2005) 455–460. https://doi.org/10.1016/j.scriptamat.2004.11.010.

[85] R.M. German, Sintering: From Empirical Observations to Scientific Principles, 2014. https://doi.org/10.1016/B978-0-12-401682-8.00001-X.

[86] R.M. German, Sintering Theory and Practice, John Wiley & Sons, New York, 1996.

[87] J.K. Mackenzie, R. Shuttleworth, A Phenomenological Theory of Sintering, Proc. Phys. Soc. Sect. B. (1949) 833–852. https://doi.org/10.1016/S0020-7101(96)90005-7.

[88] E.A. Olevsky, Theory of sintering: from discrete to continuum, Mater. Sci. Eng. R. 23 (1998) 41–100.

[89] F.A. Nichols, Theory of sintering of wires by surface diffusion, Acta Metall. 16 (1968) 103–113. https://doi.org/10.1016/0001-6160(68)90079-5.

[90] H. Djohari, J.I. Martínez-Herrera, J.J. Derby, Transport mechanisms and densification during sintering: I. Viscous flow versus vacancy diffusion, Chem. Eng. Sci. 64 (2009) 3799–3809. https://doi.org/10.1016/J.CES.2009.05.018.

[91] H. Djohari, J.J. Derby, Transport mechanisms and densification during sintering: II. Grain boundaries, Chem. Eng. Sci. 64 (2009) 3810–3816. https://doi.org/10.1016/j.ces.2009.05.022.

[92] J.H. Dedrick, A. Gerds, A study of the mechanism of sintering of metallic particles, J. Appl. Phys. 20 (1949) 1042–1044. https://doi.org/10.1063/1.1698271.

[93] R.L. Coble, Sintering crystalline solids. I. intermediate and final state diffusion models, J. Appl. Phys. 32 (1961) 787–792. https://doi.org/10.1063/1.1736107.

[94] R.L. Coble, Sintering crystalline solids. II. experimental test of diffusion models in powder compacts, J. Appl. Phys. 32 (1961) 793–799. https://doi.org/10.1063/1.1736108.

[95] R.M. German, Chapter Six - Geometric Trajectories during Sintering, in: R.M. German (Ed.), Sinter. from Empir. Obs. to Sci. Princ., Butterworth-Heinemann, Boston, 2014: pp. 141–181. https://doi.org/10.1016/B978-0-12-401682-8.00006-9.

[96] NPTEL :: Metallurgy and Material Science - Advanced ceramics for strategic applications, (n.d.). https://nptel.ac.in/courses/113105015/ (accessed November 2, 2018).

[97] C. You, C. Luan, X. Wang, An evaluation of solid bridge force using penetration to measure rheological properties, Powder Technol. 239 (2013) 175–182. https://doi.org/10.1016/j.powtec.2013.01.066.

[98] E. Torresani, D. Giuntini, C. Zhu, T. Harrington, K.S. Vecchio, A. Molinari, R.K. Bordia, E.A. Olevsky, Anisotropy of Mass Transfer During Sintering of Powder Materials with Pore–Particle Structure Orientation, Metall. Mater. Trans. A Phys. Metall. Mater. Sci. 50 (2019) 1033–1049. https://doi.org/10.1007/s11661-018-5037-x.

[99] E.W. Hart, On the role of dislocations in bulk diffusion, Acta Metall. 5 (1957) 597. https://doi.org/10.1016/0001-6160(57)90127-X.

[100] A. Molinari, C. Menapace, E. Torresani, I. Cristofolini, M. Larsson, Working hypothesis for origin of anisotropic sintering shrinkage caused by prior uniaxial cold compaction, Powder Metall. 56 (2013) 189–195. https://doi.org/10.1179/1743290112Y.0000000043.

[101] J. Wendel, S.K. Manchili, E. Hryha, L. Nyborg, Sintering behaviour of compacted water-atomised iron powder: effect of initial state and processing conditions, Powder Metall. 63 (2020) 338–348. https://doi.org/10.1080/00325899.2020.1833138.

[102] J. Wendel, S.K. Manchili, Y. Cao, E. Hryha, L. Nyborg, Evolution of surface chemistry during sintering of water-atomized iron and low-alloyed steel powder, Surf. Interface Anal. (2020) 1–5. https://doi.org/10.1002/sia.6852.

[103] O. Dominguez, Y. Champion, J. Bigot, Liquidlike Sintering Behavior of Nanometric Fe and Cu Powders: Experimental Approach, Metall. Mater. Trans. A Phys. Metall. Mater. Sci. 29 (1998) 2941–2949. https://doi.org/10.1007/s11661-998-0201-3.

[104] K.K. Nanda, Size-dependent melting of nanoparticles: Hundred years of Thermodynamic model, Pramana - J. Phys. 72 (2009) 617–628. https://doi.org/10.1007/s12043-009-0055-2.

[105] P. P, Ober die Abhängigkeit des Schmelzpunktes von der Oberflächenenergie eines festen Körpers (Zusatz.), Zeitschrift Für Phys. Chemie. 65U (1909) 545. https://doi.org/10.1515/zpch-1909-6532.

[106] P. Buffat, J.-P. Borel, Size effect on the melting temperature of gold particles, Physic Al Rev. a Vol. 13 (1976) 2287–2298.

[107] P. Couchman, W.A. Jesser, Thermodynamic theory of size dependence of melting temperature in metals, Nature. 270 (1977) 572. https://doi.org/10.1038/266309a0.

[108] P. Jena, B.K. Rao, S.N. Khanna, The Physics and Chemistry of Small Clusters, Plenum Press, New York, 1987.

[109] J.R. Groza, Nanosintering, Nanostructured Mater. 12 (1999) 987–992. https://doi.org/10.1016/S0965-9773(99)00284-6.

[110] O. Dominguez, M. Phillippot, J. Bigot, The relationship between consolidation behavior and particle size in Fe nanometric powders, Scr. Metall. Mater. 32 (1995) 13–17. https://doi.org/10.1016/S0956-716X(99)80003-X.

[111] J. Rajabi, N. Muhamad, A.B. Sulong, Effect of nano-sized powders on powder injection molding: a review, Microsyst. Technol. 18 (2012) 1941–1961. https://doi.org/10.1007/s00542-012-1631-9.

[112] J.R. Groza, Nanosintering, Nanostructured Mater. 12 (1999) 987–992. https://doi.org/10.1016/S0965-9773(99)00284-6.

[113] J.W. Oh, R. Bollina, W.S. Lee, S.J. Park, Effect of nanopowder ratio in bimodal powder mixture on powder injection molding, Powder Technol. 302 (2016) 168–176. https://doi.org/10.1016/j.powtec.2016.08.051.

[114] Y.S. Kang, B.H. Cha, H.G. Kang, J.S. Lee, Densification behavior and microstructural development of nano-agglomerate powder during sintering, Mater. Sci. Forum. 534–536 (n.d.) 505–8. http://dx.doi.org/10.4028/www.scientific.net/MSF.534-536.505.

[115] J.W. Oh, S.K. Ryu, W.S. Lee, S.J. Park, Analysis of compaction and sintering behavior of 316L stainless steel nano/micro bimodal powder, Powder Technol. 322 (2017) 1–8. https://doi.org/10.1016/j.powtec.2017.08.055.

[116] D. Wei, R. Dave, R. Pfeffer, Mixing and Characterization of Nanosized Powders: An Assessment of Different Techniques, J. Nanoparticle Res. 4 (2002) 21–41. https://doi.org/10.1023/A:1020184524538.

[117] J. Fruhstorfer, S. Schafföner, C.G. Aneziris, Dry ball mixing and deagglomeration of alumina and zirconia composite fine powders using a bimodal ball size distribution, Ceram. Int. 40 (2014) 15293–15302. https://doi.org/10.1016/j.ceramint.2014.07.027.

[118] J. Wendel, R. Shvab, Y. Cao, E. Hryha, L. Nyborg, Surface analysis of fine water-atomized iron powder and sintered material, Surf. Interface Anal. 50 (2018) 1065–1071. https://doi.org/10.1002/sia.6455.

[119] E. Hryha, L. Nyborg, Oxide Transformation in Cr-Mn-Prealloyed Sintered Steels: Thermodynamic and Kinetic Aspects, Metall. Mater. Trans. A. 45 (2014) 1736–1747. https://doi.org/10.1007/s11661-013-1969-3.

[120] D. Chasoglou, E. Hryha, M. Norell, L. Nyborg, Characterization of surface oxides on water-atomized steel powder by XPS/AES depth profiling and nano-scale lateral surface analysis, Appl. Surf. Sci. 268 (2013) 496–506. /https://doi.org/10.1016/j.apsusc.2012.12.155.

[121] P.J. Haines, Thermogravimetry, in: Therm. Methods Anal. Princ. Appl. Probl., Springer Netherlands, Dordrecht, 1995: pp. 22–62. https://doi.org/10.1007/978-94-011-1324-3_2.

[122] H. Bhadeshia, Dilatometry, (n.d.). https://www.phase-trans.msm.cam.ac.uk/2002/Thermal3.pdf (accessed October 15, 2018).

[123] J. Moulder, W. Stickle, P. Sobol, K. Bomben, X-ray photoelectron spectroscopy (XPS), Handb. X-Ray Photoelectron Spectrosc. (1992). https://doi.org/10.1002/0470014229.ch22.

[124] Swathi K. Manchili, Role of nanopowder as sintering aid in the densification of water atomized ferrous powder, 2018.

[125] J.B. Lumsden, X-Ray Photoelectron Spectroscopy, in: Mater. Charact., ASM International, 1986. https://doi.org/10.31399/asm.hb.v10.a0001771.

[126] R. Simpson, R.G. White, J.F. Watts, M.A. Baker, Applied Surface Science XPS investigation of monatomic and cluster argon ion sputtering of tantalum pentoxide, Appl. Phys. Lett. 405 (2017) 79–87. https://doi.org/10.1016/j.apsusc.2017.02.006.

[127] W.E.S. Unger, T. Wirth, V.D. Hodoroaba, Auger electron spectroscopy, Elsevier Inc., 2019. https://doi.org/10.1016/B978-0-12-814182-3.00020-1.

[128] D. Chasoglou, E. Hryha, L. Nyborg, Effect of Sintering Atmosphere on the Transformation of Surface Oxides During the Sintering of Chromium Alloyed Steel, 2010.

[129] M. Norell, L. Nyborg, T. Tunberg, I. Olefjord, Thickness determination of surface oxides on metal powder by AES depth profiling, Surf. Interface Anal. 19 (1992) 71–76. https://doi.org/10.1002/sia.740190116.

[130] S.J. Pennycook, Transmission Electron Microscopy, in: F. Bassani, G.L. Liedl, P. Wyder (Eds.), Encycl. Condens. Matter Phys., Elsevier, Oxford, 2005: pp. 240–247. https://doi.org/10.1016/B0-12-369401-9/00582-9.

[131] P. Sciau, Chapter Two - Transmission Electron Microscopy: Emerging Investigations for Cultural Heritage Materials, in: P.W. Hawkes (Ed.), Elsevier, 2016: pp. 43–67. /https://doi.org/10.1016/bs.aiep.2016.09.002.

[132] R. Kohli, K.L. Mittal, eds., Chapter 3 - Methods for Assessing Surface Cleanliness, in: Dev. Surf. Contam. Cleaning, Vol. 12, Elsevier, 2019: pp. 23–105. https://doi.org/10.1016/B978-0-12-816081-7.00003-6.

[133] J. Schindelin, I. Arganda-Carreras, E. Frise, V. Kaynig, M. Longair, T. Pietzsch, S. Preibisch, C. Rueden, S. Saalfeld, B. Schmid, J.-Y. Tinevez, D.J. White, V. Hartenstein, K. Eliceiri, P. Tomancak, A. Cardona, Fiji: an open-source platform for biological-image analysis, Nat. Methods. 9 (2012) 676–682. https://doi.org/10.1038/nmeth.2019.

[134] I. Arganda-Carreras, V. Kaynig, C. Rueden, K.W. Eliceiri, J. Schindelin, A. Cardona, H. Sebastian Seung, Trainable Weka Segmentation: a machine learning tool for microscopy pixel classification, Bioinformatics. 33 (2017) 2424–2426. https://doi.org/10.1093/bioinformatics/btx180.

[135] Y.-S. Rhee, S.-Y. Chang, C.-W. Park, S.-C. Chi, E.-S. Park, Optimization of ibuprofen gel formulations using experimental design technique for enhanced transdermal penetration, Int. J. Pharm. 364 (2008) 14–20. https://doi.org/10.1016/j.ijpharm.2008.07.029.

[136] M. Mohai, I. Bert, Calculation of overlayer thickness on curved surfaces based on XPS intensities, Surf. Interface Anal. 36 (2004) 805–808. https://doi.org/10.1002/sia.1769.

[137] M. Mohai, XPS MultiQuant : multimodel XPS quantification software, Surf. Interface Anal. 2 (2004) 828–832. https://doi.org/10.1002/sia.1775.

[138] A.G. Shard, A Straightforward Method For Interpreting XPS Data From Core −shell nanoparticles, J. Phys. Chem. Chysical Chem. C. 116 (2012) 16806–16813. https://doi.org/10.1021/jp305267d.